Spring 1-1-2016

Effects of Right Ventricular Diastolic Dysfunction on Coherent Flow Structures in the Human Right Atrium and Right Ventricle

James R. Browning
University of Colorado at Boulder, jameybrowning@gmail.com

EFFECTS OF RIGHT VENTRICULAR DIASTOLIC DYSFUNCTION ON COHERENT FLOW STRUCTURES IN THE HUMAN RIGHT ATRIUM AND RIGHT VENTRICLE

James R. Browning

B.S., University of Massachusetts Amherst, 2006

M.S. University of Massachusetts Amherst, 2009

A thesis submitted to the Faculty of the Graduate School of the University of Colorado

in partial fulfillment of the requirement for the degree of

Doctor of Philosophy

Department of Mechanical Engineering

2016

Signature Page

This thesis entitled:
Effects of Right Ventricular Diastolic Dysfunction on Coherent Flow Structures in the Human Right Atrium and Right Ventricle

written by James R. Browning
has been approved for the Department of Mechanical Engineering

_____
(Jean Hertzberg)

_____
(Brett Fenster)

Date_____

The final copy of this thesis has been examined by the signatories, and we find that both the content and the form meet acceptable presentation standards of scholarly work in the above mentioned discipline.

National Jewish Health IRB Protocol # __2808____

ABSTRACT

Browning, James Robert (Ph.D., Mechanical Engineering)

Effects of Right Ventricular Diastolic Dysfunction on Coherent Flow Structures in the Human Right Atrium and Right Ventricle

Thesis directed by Associate Professor Jean Hertzberg

Heart disease, the leading cause of death in the US, is a complex pathology which may manifest in several ways including morphological and hemodynamic changes in the heart and circulatory system. Recent advances in time resolved cardiac magnetic resonance imaging (4DMRI) have allowed for characterization of blood flow in the right ventricle (RV) and right atrium (RA), including calculation of vorticity and circulation, and qualitative visual assessment of coherent flow patterns. This thesis presents background on heart disease, specifically right ventricular diastolic dysfunction (RVDD), and 4DMRI tools and techniques used for quantitative and qualitative analysis of cardiac flows in the normal and disease states. Results of a preliminary study of right heart vorticity in subjects with RVDD are presented which inform the direction of later analysis. 4DMRI data is characterized to evaluate its suitability for quantitative and qualitative study of the RVDD pathology. Results of a 34 subject study or 20 RVDD patient and 14 normals are presented in which a significant difference is found in early diastolic right heart vorticity between the normal and pathologic group. A qualitative visual analysis is presented of differences and similarities in 3D flow structures between a single normal and RVDD subject at peak systole, peak early diastole, and late diastole in which several differences in 3D flow are

observed. The thesis ends with observations regarding right heart three-dimensional flow characteristics of the RVDD pathology and the use of 4DMRI as a research tool for the study of right heart pathologies.

NOMENCLATURE

4DMRI	three-dimensional time resolved magnetic resonance imaging
BAV	bicuspid aortic valve
BSA	body surface area
CI	cardiac index
EDV	end diastolic volume
EF	ventricular ejection fraction
ESV	end systolic volume
IVC	inferior vena cava
lPA	left pulmonary artery
LV	left ventricle
MPA	main pulmonary artery
PAH	pulmonary arterial hypertension
PFR	peak filling rate
PHT	normal LV function with PAH
ρ_c	concordance coefficient of interobserver reliability
rPA	right pulmonary artery
ROI	region of interest
RV	right ventricle
RVEDV	right ventricular end diastolic volume
RVDD	right ventricular diastolic dysfunction
RVM	right ventricle mass
RVOT	right ventricular outflow tract
SS	integrated vorticity CI scaling method
SVC	superior vena cava
TS	vorticity threshold CI scaling method
TV	tricuspid valve
VSS	velocity sum-of-squares segmentation

CONTENTS

TABLES

FIGURES

1. Motivation

According to the US Centers for Disease Control and Prevention, heart disease was the leading cause of death in 2012 (the most recent year for statistics) accounting for 599,711 deaths, or 23.6% of total deaths (Heron et al. 2015). Although the death rate due to heart disease has been steadily declining since 1980, the continuing incidence of cardiac pathologies still remains an important public health challenge. In 2006, a National Heart, Lung and Blood Institute working group identified the role of the right heart in heart disease as a high research priority for the National Institutes of Health (Voelkel et al. 2006). The working group identified several areas of deficient understanding including functional measurement, the effect of pulmonary disease on right ventricular function, and models of right ventricular failure.

With these needs in mind, we studied the effects of human right ventricular diastolic dysfunction (RVDD) on the hemodynamics of the right heart, including the right atrium (RA) and right ventricle (RV), using 3-dimensional time-resolved phase contrast cardiac magnetic resonance (4DMRI) data sets from both healthy controls and subjects diagnosed with RVDD. In particular, we focused on the qualitative and quantitative characteristics of coherent flow structures present in the right heart during vectricular diastole. This program of research has three ultimate goals; 1) Elucidate the role of coherent flow structures in the function, dysfunction, and failure of the right heart, 2) Improved diagnostics for right heart pathologies, and 3) The development of tools and techniques for assessing right heart function using 4DCMR.

2. Background

2.1. Physiology and Pathology of RVDD

Right ventricle diastolic dysfunction occurs when right ventricle diastolic relaxation is impeded. In order to provide a physiological description of RVDD, as well as a physiological and pathological context for the dysfunction, the following sections will provide background on the physiology of the healthy human heart, an overview of heart failure and heart disease, and the role of RV function in heart disease and failure.

2.1.1. The Normal Functioning Heart

The human heart is a muscular organ that can be thought of as consisting of two sides, the right heart and the left heart, each of which consist of (moving downstream) an atrium, a one-way atrial-ventricular check valve, a ventricle, and an additional check valve leading to the main pulmonary artery or the ascending aortic artery for the right and left sides of the heart respectively. The cardiac cycle can be divided into three primary intervals; systole, the contraction of the ventricles; early (E) diastole, the relaxation of the ventricles; and late (A) diastole, the contraction of the atria.

Starting with the right side of the heart, a pressure gradient causes deoxygenated blood to flow from the superior vena cava (SVC) and inferior vena cava (IVC) into the RA during the beginning of the cardiac cycle, systole (See Figure 1). The RV then relaxes during the early diastolic (E-wave) interval in the cardiac cycle, causing a positive pressure gradient between the RV and RA, and blood flows in the RV from the RA through the tricuspid valve (TV) which acts as a one way check valve. Following early diastole, the RA contracts, further filling the RV with blood during the late diastolic interval of the cardiac cycle. At this point, systole begins again and while the RA is again filling, the RV contracts, the TV closes, and deoxygenated blood is pumped from the RV, through the pulmonary valve, through the main

pulmonary artery (MPA) which branches into the right and left pulmonary arteries through which blood is pumped through the right and left lungs where it is oxygenated via molecular diffusion.

The left heart functions similarly to the right heart, but instead of pumping deoxygenated blood through the lungs, it is responsible for pumping oxygen rich blood throughout the body. Again starting with systole, oxygen rich blood flows from the left and right pulmonary veins into the left atrium (LA). In early diastole, the left ventricle (LV) relaxes, drawing blood through the mitral valve. During late diastole, the LA contracts pumping additional blood into the LV. During systole, the LV contracts, pumping blood through the aortic valve and then through the ascending aorta where it is then dispersed throughout the body via a system of branching arteries.

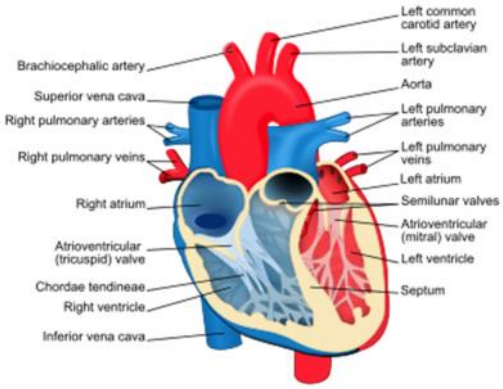

Figure 1. Schematic of the human heart

2.1.2.Heart Failure and Heart Disease

For each side of the heart, heart failure can be divided into two broad categories; systolic failure and diastolic failure ("Types of Heart Failure" 2014). Systolic failure occurs due to a dysfunction of the ventricle in which it is not able to contract with enough force to adequately pump blood through the circulatory system. Diastolic failure occurs when the ventricle is not able to draw an adequate volume of blood during early diastolic relaxation. Diastolic dysfunction and failure is generally caused by loss of

tissue compliance (a passive property of heart tissue) and/or lessening of myocardial relaxation (an active property of heart tissue) (Schwarz and Dashti 2010). Systolic dysfunction and failure is characterized by an increase in ventricular volumes throughout the cardiac cycle, decreased wall thickness, and a resulting reduced ejection fraction (the fraction of blood pumped from the ventricle during systolic contraction) (Chatterjee and Massie 2007). In either case, the volume of blood pumped through the heart is less than that required by the body; either through a decreased ejection fraction (systolic failure) or a normal ejection fraction coupled with a lower volume of blood in the ventricle (diastolic failure).

2.1.3.The General Role of RV Function in Heart Disease

Common symptoms of RV failure include fluid retention leading to edema, low cardiac output leading to fatigue and intolerance to exercise, and right heart arrhythmias. RV dysfunction commonly refers to systolic (contractile) or diastolic (filling) dysfunctions (Haddad et al. 2008). The abundant mechanisms and causes of right heart failure have been classified into several categories; volume overload, pressure overload, myocardial ischemia and infarction, intrinsic myocardial processes, inflow limitations, complex congenital defects, and pericardial disease.

The most common cause of right heart pressure overload is left heart failure, illustrating the close relationship between left and right heart functioning. Figure 2 shows a highly simplified schematic of the circulatory system with the heart in greater detail in the center. When viewed as a closed loop, a reduction in pressure in the aorta due to left heart systolic dysfunction will eventually lead to a reduction in pressure at the IVC and SVC, and thus the RA and RV will be less able to fill with blood during diastole. Similarly, a lack of fluid being drawn into the LV because of left heart diastolic dysfunction will result in a buildup of fluid and pressure in the lungs and MPA, resulting in higher

pressures in the right ventricle during systole – which will eventually lead to RV systolic dysfunctions and possibly failure (Haddad et al. 2008).

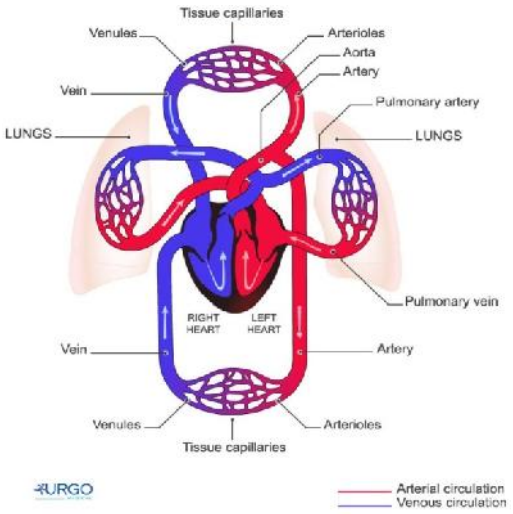

Figure 2. Simplified schematic of the circulatory system (Source: URGO Medical. www.urgomedical.com)

Causes of right heart volume overload include tricuspid and pulmonary valve regurgitation, and morphological defects such as coronary artery fistulas into the RV or RA, pulmonary venous return, and atrial septal defects.

Haddad et al. suggest a four stage progressive scale for the development of RV failure, ranging from at risk for RV dysfunction at stage 1, to RV failure requiring specialized interventions at stage 4. Management goals range from monitoring of heart function and lifestyle changes for stage 1 patients to transplants and mechanical assist devices for stage 4.

2.1.4. RV Diastolic Function in Heart Failure

Right ventricle diastolic function is often present in heart failure patients. A study of 145 subjects with either symptomatic heart failure or PHT (normal LV function with pulmonary arterial hypertension

(PAH)) showed a high prevalence of RV diastolic abnormalities including lower tricuspid E/A ratios (the ratio of early (E-wave) and late (A-wave) diastolic RV filling), lower peak E-wave velocity, and longer RV relaxation time (Yu et al. 1996). The same study found these RV diastolic parameters correlated strongly with PAH in the PHT group, but that within the symptomatic heart failure group, only RV E-wave deceleration time (the time from peak E-wave velocity to subsequent baseline) correlated with PAH indicating that RVDD is not due only to elevated pulmonary arterial pressure.

2.2. Cardiac 4DMRI studies

Magnetic resonance imaging is used for both clinical and research applications in the right and left heart, including phase contrast (velocity) imaging, tissue contrast imaging, and a combination of both. This section provides a brief history of cardiac 4DMRI focusing primarily on research aspects. The section begins with a general overview of cardiac specific 4DMRI studies, moves on to 4DMRI studies of the normal left and right heart, and ends with studies of the pathological left and right heart.

2.2.1. Cardiac Specific 4DMRI

Current cardiac flow visualization and analysis technologies include echocardiographic imaging and 4DMRI. The advantages of echocardiographic imaging include low cost, wide availability, real-time data generation, and instantaneous (rather than time averaged) velocity data. The primary disadvantage is that echocardiography is essentially a 2D flow field technique, and thus has limitations in describing the behavior of the 3D cardiac flow fields. 4DMRI by contrast, is able to resolve 3D flow fields, however, it is more expensive and in clinical settings relies on time-averaging flow data rather than recording instantaneous velocity measurements (Rodriguez Munoz et al. 2013).

MRI has been used for imaging cardiac flow velocities since at least the early 1980's (Moran 1982). Since then, applications for cardiac 4DMRI have multiplied and the technology has now been used for

characterizing several abnormal cardiac flows. Markl et al. lists 20 peer reviewed studies with publication dates ranging from 1993-2010 which used 4DMRI for analysis of cardiac flows (Markl, Kilner, and Ebbers 2011).

Current challenges to the widespread adoption of cardiac 4DMRI include scan times that can be uncomfortable for patients with cardiac illness, low spatial and time resolution, the necessity of complex post-processing of the raw velocity and tissue contrast images, and the lack of clinically relevant methods of visualizing and analyzing large 3D velocity data sets. Spatial and temporal resolution of 2mm and 40ms over the volume of the heart currently requires a 20-30 minute scan-time which can be challenging for a sick patient who is required to lie still in the supine position during the scan (Markl, Kilner, and Ebbers 2011). Even at these spatial resolutions, flow characteristics such as wall shear stress (WSS) can be difficult to resolve. A typical cardiac 4DMRI heart scan may include data for tissue contrast plus 3 velocity components within a 116x116x40 pixel 3D grid (roughly 500,000 pixels) for a total of several million data points per scan.

2.2.2.Normal Left Heart 4DMRI Studies

Due to the perceived importance of the left heart in overall cardiac health and illness, as well as the more regular geometry of the left ventricle, many studies have been published which use 4DMRI to characterize blood flow in the left heart, including the aortic artery. In 2000, Kilner et al. used 4DMRI images in 5 coronal slices throughout the left heart to describe non-symmetric 3D flows through the LA and LV. They hypothesized that the precise flow patterns in the heart may have dynamic advantages such as minimization of energy dissipation during ventricular filling and contraction (Kilner et al. 2000). Later, a collaboration between UC San Francisco and Linkoping University used 4DMRI velocity data to calculate the dissipation of kinetic energy in the LV inflow during diastole. With 17 normal subjects, the researchers found that $16 \pm 8\%$ of the kinetic energy of the inflowing fluid was conserved until the end of

diastole. By comparison, only 5% was conserved in a single subjected with mildly dilated cardiomyopathy (Bolger et al. 2007).

More recently, cardiac 4DMRI was used by Eriksson et al., in another UC San Francisco and Linkoping University collaboration, to separate the LV inflow into 4 categories - direct flow, retained inflow, delayed ejection flow, and residual volume - based on a semi-automatic fluid pathline analysis (Eriksson et al. 2010). The results of the nine subject study showed that 17$\pm$4% of blood in the LV is delayed ejection, i.e. it is contained in the LV for at least two cardiac cycles. 35$\pm$6% was direct flow, i.e. the blood entered the LV during diastole and exited during systole of the same heartbeat. The researchers note that direct flow blood volumes best retain kinetic energy throughout the diastolic-systolic cycle, while the retained inflow (blood that is retained in the LV for one cardiac cycle) and delayed ejection loses kinetic energy. Also in 2010, Bollache et al. published an automated MRI based method for evaluating left ventricular diastolic function (Bollache et al. 2010). Interoperator variability and a comparison to echocardiography was calculated for tissue velocity and blood flow parameters commonly used for their prognostic value for diastolic dysfunction including transmitral blood flowrates and peak velocities, isovolumetric relaxation time, and myocardial longitudinal velocities. The 53 subject study generally showed low interoperator variability and high agreement with same-day echocardiography results. Although the method required some manual steps, such as tracing a rough region of interest around the mitral plane, the precise locating of the mitral outflow area, as well as local peaks in the resulting velocity data, were automated, indicating a potential clinical application for automated MRI cardiac diagnostic methods.

More recent 4DMRI studies of the left ventricle have looked at coherent flows, specifically vortices in the LA and LV. In a workshop presentation, researchers from Yale University demonstrated the existence of both diastolic and systolic right atrial vortices using 4DMRI scans of healthy volunteers. In the

complete LA+LV volume, they found a total of four rotating structures which they present using streamlines superimposed on 2D planes colormapped by vorticity (Pal et al. 2012). At the same workshop, researchers from the US and Sweden presented a method of quantifying LV vortex ring formation using 4DMRI data and lagrangian coherent structures (LCS). Using LCS, they were able to calculate an LV vortex ring volume of $51 \pm 6\%$ of the total LV volume in nine healthy volunteers, and 23% in a single patient with dilated ischemic cardiomyopathy, indicating a relationship between LV ring vortex size and a single cardiac pathology (Toger et al. 2012).

2.2.3.Normal Right Heart 4DMRI studies

In comparison to left heart 4DMRI studies, right heart studies are less common, and are relatively more recent.

A 2006 British study of 120 healthy volunteers, aged 20-80 with equal numbers male and female, used CMR to develop healthy baseline parameters of the right ventricle including end diastolic and end systolic volumes (EDV and ESV), ejection fraction (EF), early peak filling rate (PFR_E), active peak filling rate (PFR_A), and right ventricle mass (RVM). All parameters were reported as both absolute and normalized to body surface area (BSA) (Maceira et al. 2006). In 2011, the UC San Francisco/ Linkoping University group used a similar technique to their 2010 left ventricle study to examine direct flow, retained inflow, delayed ejection flow, and residual volume in the right ventricle (Fredriksson et al. 2011). The three main conclusions from the paper were that the RV direct flow followed a direct path that did not extend into the apex of the RV, that the RV direct flow had larger volume and more kinetic energy than any of the other four flow components, and that the RV direct flow comprised a larger end-diastolic volume than LV direct flow. In addition, the group noted the existence of an asymmetrical diastolic RV vortex ring similar to that found in the LV. In 2014, researchers in the Netherlands used a $Lamda_2$ vortex identification method to compare RV and LV diastolic vortices. For each of the ten

subjects, parameters including longitudinal position, orientation, and circularity index was calculated for LV and RV late and early diastolic vortex rings. Vortex rings were present for all subjects, in both ventricles, and for all filling phases. RV vortex rings tended to be closer to the axis of the atrial-ventricular valve and more elliptical than LV rings (ElBaz et al. 2014).

2.2.4.Diseased/Abnormal Left Heart 4DMRI Studies

Several studies have used 4DMRI flow data to investigate abnormalities in flow coincident with cardiac pathologies, many of which focus on flow in the aorta. In 2008, researchers from UC San Francisco and Stanford University School of Medicine used 4DMRI data to examine abnormalities in aortic flow in a 14-year-old boy with a bicuspid aortic valve (BAV) (as opposed to the normal three leaflets) and aortic coarctation (narrowing of the aorta in the region of the aortic arch) (Hope et al. 2008). Using 3D visualizations of streamlines in the aorta, they found a disturbance in the flow just downstream of the coarctation, as well as two discrete nested helices that had not been previously reported with BAV. In 2010, the same group further validated the nested helix abnormality with a study of 53 individuals with normal and BAV in which nested aortic helical flow was seen in 15 of 20 BAV subjects, and none of the normal subjects (Hope et al. 2010).

In 2009, a research group from the University of Colorado and The Children's Hospital of Denver used 4DMRI to calculate differences in ascending aortic wall shear stress (WSS) between 15 patients with BAV and 15 normal subjects (both adults and children for both groups) (Barker, Lanning, and Shandas 2009). WSS is reported to instigate vascular remodeling, and the study found a significant difference in WSS between BAV and control groups. In 2011, researchers from the University of Wisconsin performed a similar study and found significantly increased WSS in subjects with ascending aortic dilatation compared to controls (Bieging et al. 2011). The study also found increased diastolic helical and vortical flows were associated with ascending aortic dilatation.

2.2.5.Diseased/Abnormal Right Heart 4DMRI Studies

Several studies have investigated alterations in flow patterns in patients with tetralogy of fallot (TOF) – a congenital heart defect characterized by three primary abnormalities; a septal defect (a passage in the septum between RV and LV), an overriding aorta which is located above the septal defect and receives blood from both the RV and LV, and a narrowing of the RV outflow tract which further increases preference of blood flow from the RV to the aorta. In a 2011 study of ten patients with repaired TOF and 4 healthy controls, researchers from the University Hospital Freiburg found significantly higher ratios of right to left pulmonary artery flow velocities compared to controls. In addition, they found higher systolic peak velocity in patients versus controls. (Geiger et al. 2011). In 2012, the University of Wisconsin group performed a 4DMRI flow study on 11 patients with repaired TOF, and 10 normals (Francois et al. 2012). Observed qualitative differences, using streamlines and pathlines, in right heart flow patterns included increased IVC/SVC flow during diastole than systole, increased diastolic vortical flow patterns in the RA and RV, and increased helical or vortical flow patterns in the PA. In addition, they found statistically significant differences in quantitative flow characteristics including MPA retrograde flow, resistance index, peak flow, time-to-peak flow, peak acceleration, and mean wall shear stress.

Other 4DMRI studies of the diseased right heart include investigation of acute pulmonary hypertension (high blood pressure in the pulmonary system) and fontan circulation (a surgical bypass of a non-functioning right ventricle). In 2011, the University of Wisconsin group used 4DMRI to study 3D flow patterns in the pulmonary arteries of four adult canines both before and after acute hypertension via micro-bead embolization (i.e. partial blockage of the pulmonary vasculature) (Roldán-Alzate et al. 2011). The researchers found decreased RV ejection fraction with the hypertensive subjects, and a good correlation between RV ejection fraction and MPA regional area change. In addition, flow abnormalities were noted in the hypertensive subjects including higher systolic MPA flow velocities, increased systolic

vorticity in the RV and MPA, and very low diastolic flow in the RV outflow tract. In 2011, in a collaboration between researchers at the University of Wisconsin and the University Hospital Freiburg, flow patterns in patients who had received a surgical fontan procedure were investigated using 4DMRI (Markl et al. 2011). The researchers found significantly decreased peak flow in the IVC and SVC in the four fontan patients compared to healthy controls. They also found reduced pulsatility in the caval veins and pulmonary artery. In 2015, we showed that 4D CMR-derived right heart vorticity correlates with echocardiographic indices of RVDD in a small cohort (RVDD N=13, Normal N=10) of subjects (Fenster et al. 2015).

These previous studies suggest that 4DMRI is a useful tool for investigating the fluid mechanics of pathologies of the right and left heart, using both quantitative and qualitative 4DMRI analysis techniques. 4DMRI technology and techniques allow researchers to go beyond flow measurements available with technologies such as echocardiography, to examine 3D flow structures that are sensitive to subtle changes in the cardiac physiology

2.3. Tools and Techniques

Tools and techniques used for 4DMRI flow analysis include 4DMRI data pre-processing, segmentation of cardiac features, flow visualization techniques, vortex identification and characterization, and flow metrics such as formation number. This section provides and overview of these topics, focusing on subjects relative to the research presented later.

2.3.1. 4DMRI

Phase-Contrast Magnetic Resonance Imaging (PC-MRI) is a medical imaging technique utilizing the physical phenomenon of nuclear magnetic resonance (NMR) to detect contrast between differing tissue types at different locations in the imager's field of view. Although NMR is a complex phenomenon, a

simple explanation is that the frequency of the electromagnetic radiation (ER) emitted by nuclei in a material can be altered in a predictable fashion by placing the material in magnetic fields of varying strengths. MRI makes use of this phenomenon by aligning nuclei of hydrogen isotopes in biological tissues by placing the patient in a magnetic field of spatially varying strength, perturbing the alignment with a radiofrequency pulse, and measuring the frequency and strength of the ER emitted by the hydrogen nuclei as they realign with the magnetic field. Because the frequency of the emitted ER is a function of magnetic field strength, and the magnetic field varies spatially, the location from which ER was emitted can be calculated. Because strength of the signal is a function of the density of hydrogen atoms in a material, contrast can be achieved between various tissues. Phase-contrast MRI uses phase changes in the transverse magnetization of nuclei moving relative to the scanner (changing magnetization normal to the steady magnetic gradient) to calculate the velocity of blood flow. Using magnets aligned in three directions, the three velocity components of blood flows can be calculated at each pixel (McRobbie et al. 2006).

4D PC-MRI is capable of producing magnitude (also referred to as image intensity) and three velocity components at pixels arranged in a 3D spatial grid over multiple times steps within the cardiac cycle. Typical spatial resolutions for pixels are on the order of several millimeters. Typical time resolution for 3D flow studies is on the order of 50 ms, or roughly 20 time steps within a cardiac cycle. Spatial resolution, image contrast, and time resolution must all be traded against the length of time the patient must lie still within an MRI scanner. Because 3D time resolved scans can take an hour or more, patient comfort becomes a significant factor when deciding on the quality of the images that the scanner will be programmed to acquire.

2.3.2.Data Pre-processing

Pre-processing 4DMRI data consists of noise reduction, velocity anti-aliasing, and conversion from dicom data type to a data type compatible with 3D viewers.

Noise reduction is required for phase (i.e. velocity) images due to low signal-to-noise ratio (SNR) in low signal regions of the scanned tissue, for example the lungs, which appear very dark on an MRI tissue contrast image. Removing noise allows the data to be visualized without the presence of false velocity data in these regions. Two methods for removing noise are the velocity standard deviation method and the magnitude image method. The first method involves zeroing pixels in the velocity images that have a higher temporal standard deviation than a user-defined value. For successful implementation, this method requires regions of random noise to have consistently higher temporal velocity standard deviation than blood containing regions (Walker et al. 1993). The second method is to zero velocity for pixels that have a magnitude below a defined threshold in the corresponding pixel from a tissue contrast image. Successful implementation of this method requires that noise is mostly present exclusively in regions of low tissue-contrast amplitude, and that blood containing regions have a comparably high tissue contrast magnitude (Bock et al. 2007).

When setting the parameters of a 4DMRI scan sequence, the operator needs to specify a maximum velocity encoding value (venc). Ideally, this value will be higher than any velocities expected in the subject being scanned, but low enough to provide adequate velocity resolution and sensitivity. However, if a velocity exceeds venc, the value must be wrapped in the resulting image. For example, if venc is set to $\pm$100 cm/s, a velocity of 120 cm/s is recorded as -80 cm/s, and a velocity of -110 cm/s would be recorded as 90 cm/s (Markl 2005). Aliasing may be particularly predominant in the great vessels during systole. Therefore, if aliasing is suspected, the data must be corrected either manually or with an anti-aliasing algorithm.

2.3.3.Segmentation

Cardiac segmentation refers to extraction of geometry or morphology of the cardiac chambers and arteries from 4DMRI data, which can be critical for visualization and quantitative analysis.

The anatomical data used for segmentation can include blood velocity data and tissue contrast data. Blood velocity data is generally more useful for regions and timesteps in the cardiac cycle with large blood velocities, such as the aorta during peak systole. However, blood velocity methods are less reliable in regions of lower velocities, such as the right ventricle apical region, or timesteps with lower velocity, for example the aorta during diastole. An example of a blood velocity based technique is phase-contrast magnetic resonance angiography (PC-MRA) in which areas of high velocity throughout the cardiac cycle are thresholded to produce a map of large vessels in the heart.

Methods based on high resolution cine (time resolved) tissue contrast images have the advantage of independence from blood velocity and temporal resolution equal to the temporal resolution of the cine images. A short axis image generally consists of several image planes from the apex to atrioventricular valve – with full coverage of the ventricle. A short axis image series at one timestep (early systole) is shown in Figure 3. Notice that the delineation between endocardium and epicardium (inner and outer layers of the heart respectively) are more pronounced for the LV than the thinner walled and more irregular RV, resulting in special challenges for RV segmentation.

Petitjean et al. provide an overview of ventricular segmentation methods using short-axis (orthogonal to long axis of the ventricles) 4DMRI cine images (Petitjean and Dacher 2011). They organize the methods into two classification groups; 1) the amount of prior information required for the method (a measure of user interaction) and 2) the general methodology. The amount of prior information for the methods reviewed range from no prior to strong prior, and the methodologies include region and edge based, pixel classification, deformable models, active shape and appearance models (ASM/AAM), and atlas

methods. The authors conclude that although several LV methods result in accuracy comparable to manual tracing (gold standard), RV segmentation remains a critical research topic due to irregular geometry, ill-defined boundaries, and the thinner RV cardiac muscle.

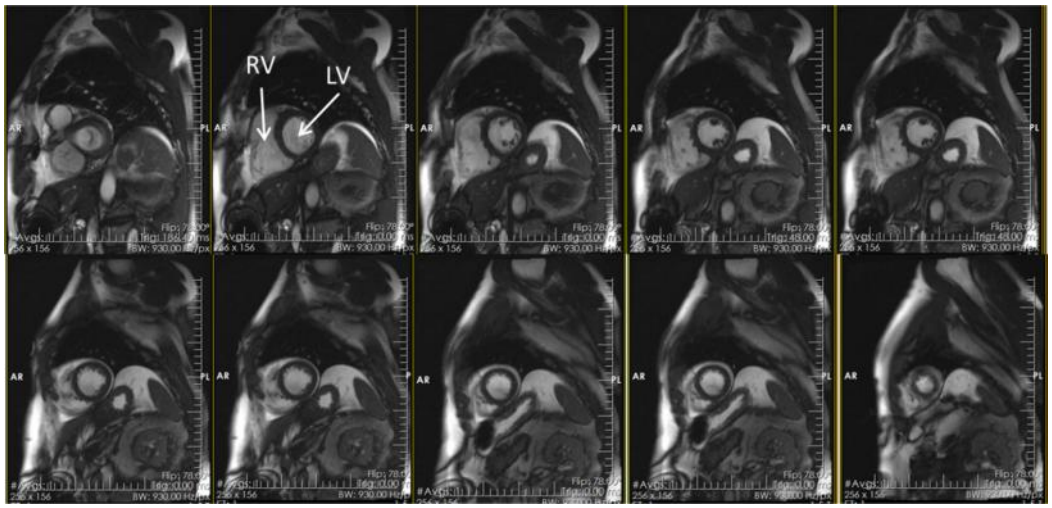

Figure 3. Short-axis cine MRI images at systole from ventricle base to apex.

In 2012, there was a right ventricle segmentation challenge at the 15th International Conference on Medical Image Computing and Computer Assisted Intervention (MICCAI) underscoring the importance and challenge of RV segmentation ("RV Segmentation Challenge in Cardiac MRI — Litislab" 2012). The winners for best automatic RV segmentation were a group from University College London using a multi-atlas approach (Zuluaga et al. 2013). The basic atlas approach requires manual locating of cardiac features, followed by automatic segmentation of the feature's boundaries. Petitjean et al. classify the multi-atlas as a strong prior information method, thus it may not be suitable for studies requiring segmentation for large numbers of subjects. Hoewever, the additional workload required of strong prior information methods may be manageable for smaller research cohorts.

2.3.4.Vortex Identification and Quantification

Vortex identification and quantification techniques in this context refer to automatic or semi-automatic methods of extracting information about vortical flows such as strength, location, and morphology, from discrete 3D vector fields. In addition to quantitative characteristics of vortical flows, vortex ID methods can be useful for visualization of vortical structures in the heart chambers and great arteries.

In a 2005 paper, Jiang et al. present an overview of nine existing vortex identification methods for 3D vector fields (Jiang, Machiraju, and Thompson 2005). The authors classify the methods based on three binaries; region/line, Galilean invariance, and local/global. The region or line designation denotes whether the methods results in a vortex core line or vortex containing region. A method is Galilean invariant if it will result in the same vortex identification in the presence or absence of a uniform velocity field. Galilean invariance is important for tracking and identifying vortices in time-varying velocity fields. The third binary, local/global, refers to the spatial information required of the algorithm. Jiang et al. consider a method local if it only requires operations in the local neighborhood of a given pixel. Methods are global if they require information from a large number of nodes, both local and non-local to a given node. In general, methods that rely on local vector derivatives and gradient tensors, such as eigenanalysis methods and vorticity methods are local, while methods that rely on streamlines, pathlines, etc. are global.

Table 1 reproduces Jiang et al.'s vortex ID taxonomy and contains the method name, authors, and classifications. Not listed, but important to note, is the pressure minimum method, which is based on the idea that a vortex will have a pressure minimum at its core due to a pressure gradient which opposes centrifugal force. Although the pressure minimum method does work for some flows, there are known instances where a pressure minimum does not occur in the core of a clearly rotating coherent

flow structure. For example, the centrifugal force of the rotating flow in a von Karman viscous pump is balanced by viscosity and does not require a lower pressure in the core (Jeong and Hussain 1995).

An ideal method for studying vortical flows in the right heart would result in a region rather than a vortex line due to the former's larger amount of information and more appropriate use for vortex visualization, would be Galilean invariant due to the time-varying nature of cardiac 4DMRI velocity fields, and be local due to ease of implementation and current challenges accurately segmenting right heart anatomical features. Of the nine methods in Table 1, the $Lambda_2$ method uniquely fits these qualifications – though other methods may still be useful for right heart 4DMRI research.

Table 1. Jiang et al.'s taxonomy of vortex ID methods.

Method Name	Authors	Line/Region	Galilean Invariant?	Local/Global
Helicity	Levy et al.	Line	No	Local
Swirl Parameter	Berdahl and Thompson	Region	No	Local
$Lambda_2$	Jeong and Hussain	Region	Yes	Local
Predictor-Corrector	Banks and Singer	Line	Yes	Global
Eigenvector	Sujundi and Haimes	Line	No	Local
Parallel Vectors	Roth and Peikert	Line	No	Local
Maximum Vorticity	Strawn et al.	Line	Yes	Local
Streamline	Sadarjoen et al.	Region	No	Global
Combinatorial	Jian et al.	Region	No	Local

The $Lambda_2$ is based on the eigenvalues of the velocity gradient tensor (Jeong and Hussain 1995). Jeong et al. begin with the premise that pressure minimum methods can fail either because: 1) unsteady

irrotational straining can create a pressure minimum in the absence of a vortex, and 2) viscosity can balance centrifugal forces within a vortex creating a vortex in the absence of a pressure minimum, as noted earlier. Jeong et al. mitigate these straining and viscous effects by considering the symmetric (S) and antisymmetric (Ω) components of the velocity gradient tensor. Figure 4 illustrates the effect on fluid flow of four local velocity gradient tensors. Note that the last two, symmetric and anti-symmetric result in pure deformation and pure rotation respectively. The Lamda$_2$ method defines a vortex as a region in which $S^2 + \Omega^2$ has exactly two negative eigenvalues. Defining J to be the velocity gradient tensor at a point, the decomposition into the symmetric and anti-symmetric parts can be calculated as

$$S = \frac{J + J^T}{2} \quad \text{and} \quad \Omega = \frac{J - J^T}{2} \tag{1}$$

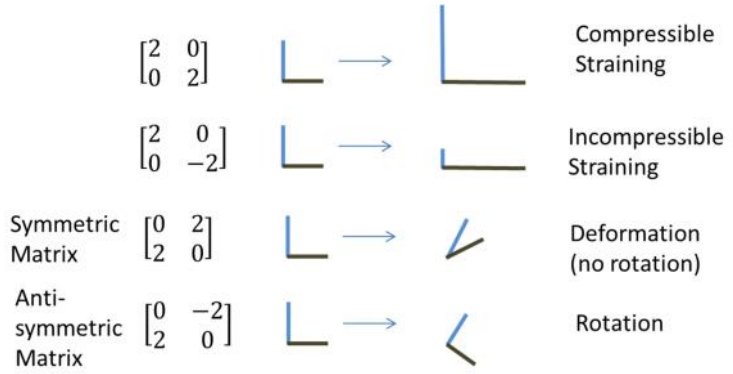

Figure 4. Four 2D velocity gradient tensors and their respective effects on fluid flow.

Recently, researchers at the University of Leiden Medical Center in the Netherlands and TU Delft used the Lambda$_2$ method to compare diastolic ventricular ring vortices in the left and right ventricles of ten healthy volunteers (ElBaz et al. 2014). After producing 3D visualizations of the resulting vortex regions, the researchers were able to note several qualitative differences in vortex characteristics between the

two ventricles, as well as between early and late diastole. The E-wave vortices were observed to be more compact, complete, and toroidal than the more elliptical and incomplete A-wave vortices. Additionally, The RV vortex rings were generally closer to the atrioventricular valve annulus, extending less far into the ventricle than the LV rings.

2.3.5. Flow Visualization

Cardiac flow visualization is a powerful clinical and research tool for understanding flow characteristics in healthy and disease states. In a 2013 review paper, Munoz et al. summarize several cardiac flow visualization technologies and techniques (Rodriguez Munoz et al. 2013). Technologies examined in this paper for acquiring blood velocity data include echocardiographic particle image velocimetry (Echo-PIV), vector flow mapping, a combination of color doppler data with speckle tracking, and 2D and 4D magnetic resonance imaging.

Echo-PIV uses ultrasound to track the location of contrast particles in two subsequent time frames, enabling a solution for particle velocity. Although useful for lower velocity applications, the method has not found widespread use for high velocity measurements in the heart due to the high frame rates required for high-velocity data acquisition. Vector flow mapping uses data from a 2D wedge shaped echo velocity acquisition and decomposes it into radial (along the ultrasound beam) and tangential (perpendicular to the beam, via the 2D continuity equation) to acquire vortical and non-vortical velocity vectors. Although the method is useful for visualizing vortical flow structures with axes normal to the acquisition plane, by using a 2D continuity equation to solve for radial flow components it requires an assumption of zero flow components normal to the acquisition plane, and thus has limited use for complex 3D flow structures. The combination Echo-PIV/flow mapping technology has shown promise for velocity data acquisition but shares the limitations inherent in the two previously mentioned echo technologies. According to Munoz et al. this technique can miss up to roughly 15% of flow when

compared to MRI technologies due to the 2D flow assumption. All echo techniques have the benefits of low cost, relative portability, wide availability, real time evaluation of flow, and relative comfort for the patient/subject.

MRI technologies are able to provide time resolved velocity data in 2D or 3D velocity fields. Because of the 4-dimensional nature (3D +time) of the data, several useful imaging techniques become possible including 2D and 3D vector fields, streamlines, and particle pathlines – the latter requiring time resolved data. However, the technology has several limitations including time averaged velocity data over multiple cardiac cycles, high cost, and potentially uncomfortable acquisition times during which an unhealthy patient must lie still in the supine position.

Techniques used to visualize 3D time-resolved velocity data include velocity and vorticity vector fields, streamlines, and particle pathlines. In addition, either 2D or 3D anatomical tissue contrast masks can be used to provide information about the cardiac anatomy in conjunction with flow visualization techniques.

Streamlines are useful for showing instantaneous flow structures, such as laminar flows, helices, and vortices, but do not show the trajectory of a particle in a time-varying flow field as a pathline would. In fact, it is important to note that a helical streamline does not prove the existence of helical flow in a time-varying velocity field (Bogren and Buonocore 2010). Velocity and vorticity vectors are useful for elucidating flow directions at a given point, and for finding vorticity generating regions of the flow, such as the walls of vessels. For all vector imaging techniques, it is often useful to threshold out vectors of small magnitude in order to qualitatively assess important flow structures.

3. Experimental Objectives

In general, we qualitatively and quantitatively describe normal and RVDD+PAH pathological flow characteristics in a cohort of subjects using 4DMRI data. The research is motivated by the need for improved non-invasive diagnostic tools for right heart pathologies and a better understanding of the RVDD+PAH disease progression and pathology.

3.1. Quantitative description of Right Heart Flow

We use several methods to quantitatively characterize coherent flow structures in the right heart during diastole for RVDD subjects and normals.

The first step in this analysis was to develop segmentation and vortex identification techniques that work with the 4DMRI data sets used in this study. Proper segmentation is vital to more accurately measure volume integrated vorticity in the RA and RV volumes, and also provides additional insight during the qualitative/visualization component of the research by providing visual cues for boundaries of cardiac structures, particularly the boundaries of the right heart chambers. Due to the large number of time resolved high resolution 2D tissue contrast images we have for each subject, we have focused on semi-automated segmentation techniques based on image intensity rather than manual methods. Because the $Lambda_2$ vortex identification method has been successfully implemented in the RV by other research groups (ElBaz et al. 2014), we have used this technique as well as Q-criterion which can be implemented along with $Lambda_2$ with minimal additional time cost.

3.2. Correlate Quantitative Characteristics of Diastolic and Sytolic RA+RV flow with RVDD

One goal of this research is to understand what flow patterns in the right heart can tell us about the RVDD+PAH pathology and disease progression. With this in mind, we propose to use the measurements

described above to correlate several quantitative flow characteristics with RVDD using data from all three cohorts in order to maximize the likelihood of statistically significant and clinically relevant results.

3.3. Qualitative Characteristics of Right Heart Flow

Using visualization techniques described in section 2.3.5, we will qualitatively describe coherent flow structures in RVDD+PAH subjects and normals during three cardiac timesteps; peak systole, peak E-wave, and peak A-wave. Flow characteristics that we have previously identified using streamlines, vorticity vectors, and velocity vectors include wall generated vorticity in the IVC/SVC, tricuspid annulus, and RVOT, helical flow in the RA, and a TV/RV diastolic vorticity ring. We present a qualitative comparison of these flow structures during the aforementioned three cardiac timesteps between a pathologic and normal subject. Aside from providing potentially important insights into the RVDD pathology, this qualitative-deductive approach will help to explain quantitative characteristics elucidated in the quantitative portion of the analysis.

4. Methodology

4.1. Introduction to Subject Cohort

Table 2 gives details of the IRB-approved study population consisted of 20 subjects with RVDD and 14 controls taken from three research cohorts referred to as Siemens, Butcher, and Translational. RVDD subjects were diagnosed per American Society of Echocardiography guidelines (McLaughlin et al. 2009) (Rudski et al. 2010). All subjects were without known coronary artery disease, significant valvular heart disease, or advanced liver disease.

2D and Doppler echocardiography were performed to obtain LV and RV parameters including early (E) and late (A) filling peak velocities, E/A ratio, early diastolic deceleration time, and lateral and septal tricuspid and mitral early (e') and late (a') diastolic velocities. Echocardiography was also used to assess right and left ventricular function, with RVDD being defined as stage I (TV E/A < .8, TV E/e' > 6, and DT > 120 ms) or stage II (TV E/A = 0.8-2.1, E/e' > 6, and DT > 120 ms) (Rudski et al. 2010).

Time-resolved phase-contrast CMR imaging was performed using a Siemens Avanti 1.5 T clinical MRI system with the subject in the supine position. The scan sequence was provided by Siemens. Voxel volumes ranged from 11.75 to 20.35 mm^3, α=15°, TE/TR=2.85/48.56 ms, venc=100-150 cm/s and temporal resolution was 50 ms. An RF-spoiled gradient echo pulse sequence, prospective ECG gating, and respiratory navigators were used as described in Markl et al. 2003). Note that because of multi-cardiac cycle time averaging of the velocity data that occurs with MRI scans, stochastic properties are not present in the final velocity data but instead represent an ensemble average over multiple cardiac cycles.

In additional to phase-contrast images, high resolution axial, short axis, 4-chamber, and 2-chamber 2D cine images were obtained. Short axis images were obtained in 8 mm increments from the ventricular

apex to beyond the tricuspid plane. Figure 5 shows the image planes covered by high resolution cine images.

Table 2. 4DMRI Subject cohorts.

Cohort Name	Number of Normal	Number of RVDD	Venc (cm/s)
Siemens	10	13	100
Butcher	4	5	150
Translational	0	2	150

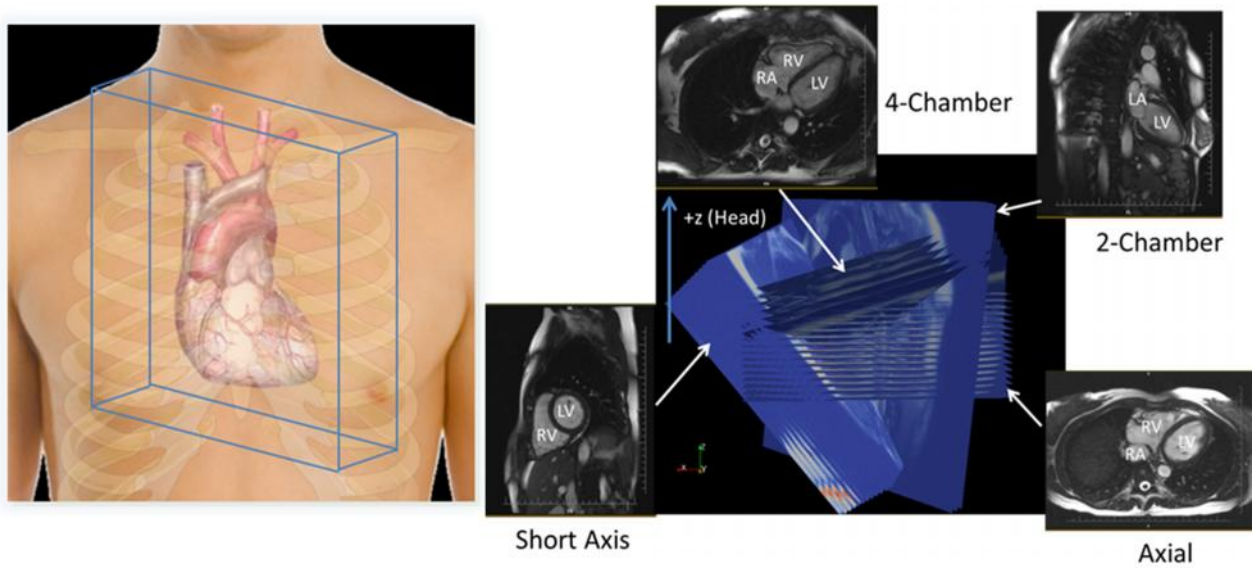

Figure 5. Orientation of 4DMRI rectangular prismatic field of view within subject's chest (Left) and orientation of a typical high-contrast, time-resolved 2D MRI image set (Right).

4.2. Preprocessing 4DMRI Data

Several 4DMRI data preprocessing tools were developed for the study of coherent cardiac flow structures including a noise reduction code, a velocity anti-aliasing algorithm, and a connected-set technique for isolating arteries from noise in PC-MRA data.

The noise reduction algorithm was based on the tissue magnitude image method described by Bock et. al. (Bock et al. 2007). A standard deviation method based on Bock's work, in which areas of high temporal RMS are filtered, was also investigated for use with 4DMRI data, but was abandoned when it was found that the method removed important data from blood-containing regions when the standard deviation was set high enough to also remove an adequate level of noise (Bock et al. 2007). Figure 6 shows an unfiltered phase contrast image, magnitude filtered velocity image, and corresponding magnitude (i.e. tissue contrast) image. Note that velocity noise is most prevalent in regions corresponding to low signal intensity of the magnitude image such as the lungs and that most of the noisy velocity pixels are removed in the filtered image. The tissue-contrast intensity threshold used for this study was set at 14 for all images which corresponds to roughly 3% of the maximum pixel intensity for the images. Velocity was set to zero in voxels corresponding to an intensity value of 14 or less in the spatially and temporally corresponding anatomical magnitude image. Visual analysis of noise filtered images for a range of thresholds and subjects showed this value to be a good compromise between noise reduction and unwanted removal of velocity data. Note that although temporally and spatially co-registered tissue contrast images are produced prior to phase contrast images during the 4DMRI scan, these images are only used in our workflow for noise filtering purposes due to their low spatial resolution relative to cine scans.

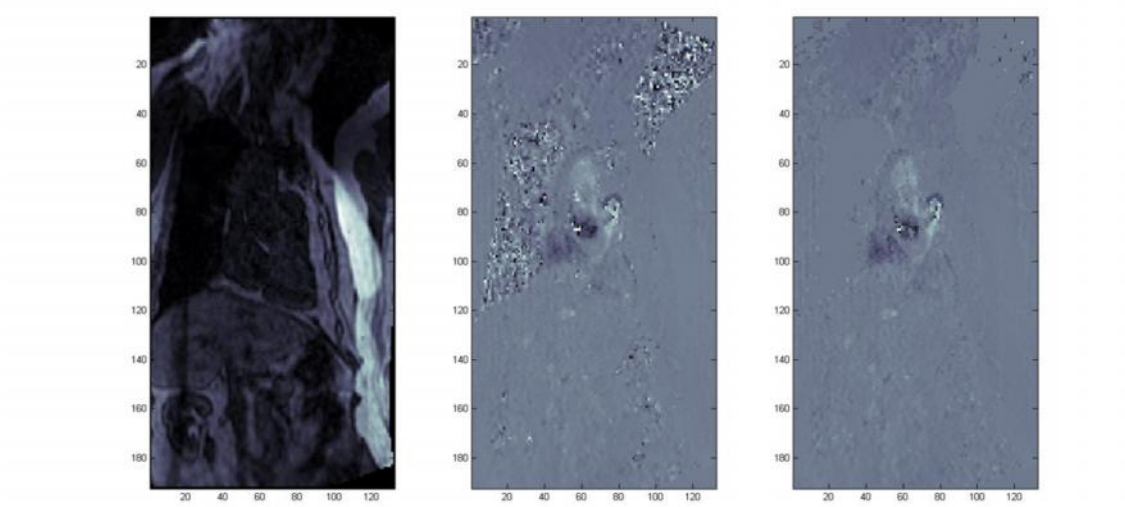

Figure 6. Still frames of magnitude (left), unfiltered i component of velocity (center), and SD/Magnitude filtered velocity for one 4DMRI image slice.

In addition to noise filtering, an anti-aliasing algorithm and code was developed. The algorithm is based on the observation that an aliased pixel, or small region of aliased pixels, will have a large velocity difference from adjacent pixels. Shown in Figure 7 is a logic chart for the anti-aliasing algorithm, and shown in Figure 8 is a representative result from several iterations of the algorithm on a heavily aliased image.

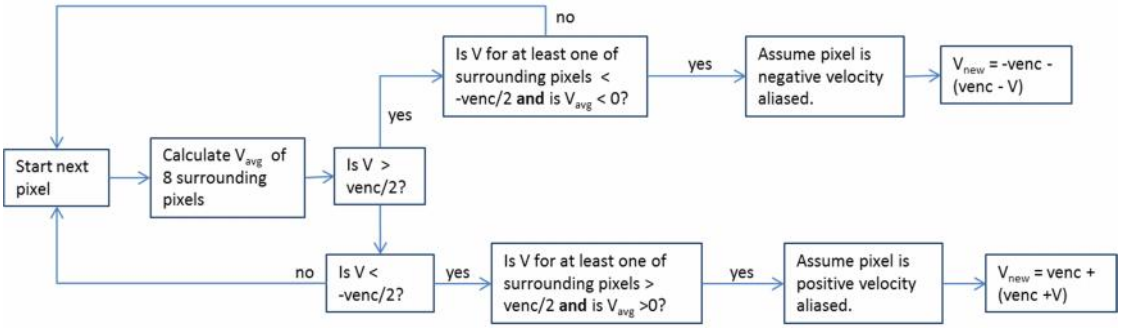

Figure 7. Anti-aliasing algorithm logic chart.

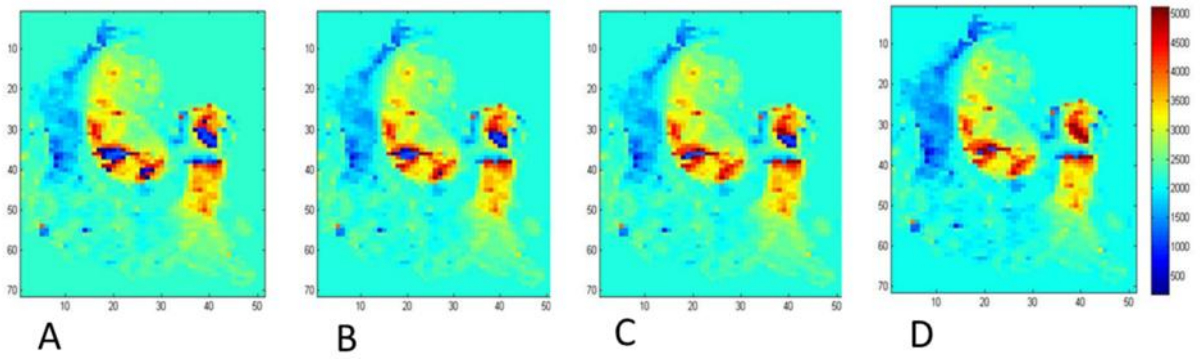

Figure 8. Results of anti-aliasing algorithm on aliased image slices of the aorta and MPA demonstrating the 1st, 2nd, 3rd, and 5th iterations of the algorithm on a heavily aliased velocity image. No further aliasing is identified by the algorithm beyond the 5th

4.3. Calculating Flowrates Through the MPA and TV

Flowrates through the tricuspid valve and pulmonary artery were calculated using 4DMRI velocity data and ParaView flow visualization software (Henderson 2004). The TV plane perpendicular to the direction of bulk blood flow was initially located visually using a cine animation of a mid-TV 4-chamber MRI tissue contrast slice at the approximate start of diastole as shown in Figure 9a. Figure 9b shows how a spherical clip was then combined with a slice of blood velocity data co-located with the TV plane to produce a disk of velocity data approximating the area of flow through the TV. The size and location of the disk was further refined by visually comparing it to velocity images in the TV plane, 3D velocity vector glyphs, and high-resolution short-axis tissue contrast images during all early diastolic timesteps (Figure 9c and d). The area-integrated normal flow through the disk was then calculated for each time step and the resulting TV flowrate time-series was exported from ParaView. Due to movement of the tricuspid annulus during diastole, this method is only accurate at the time step for which the disk position is optimized.

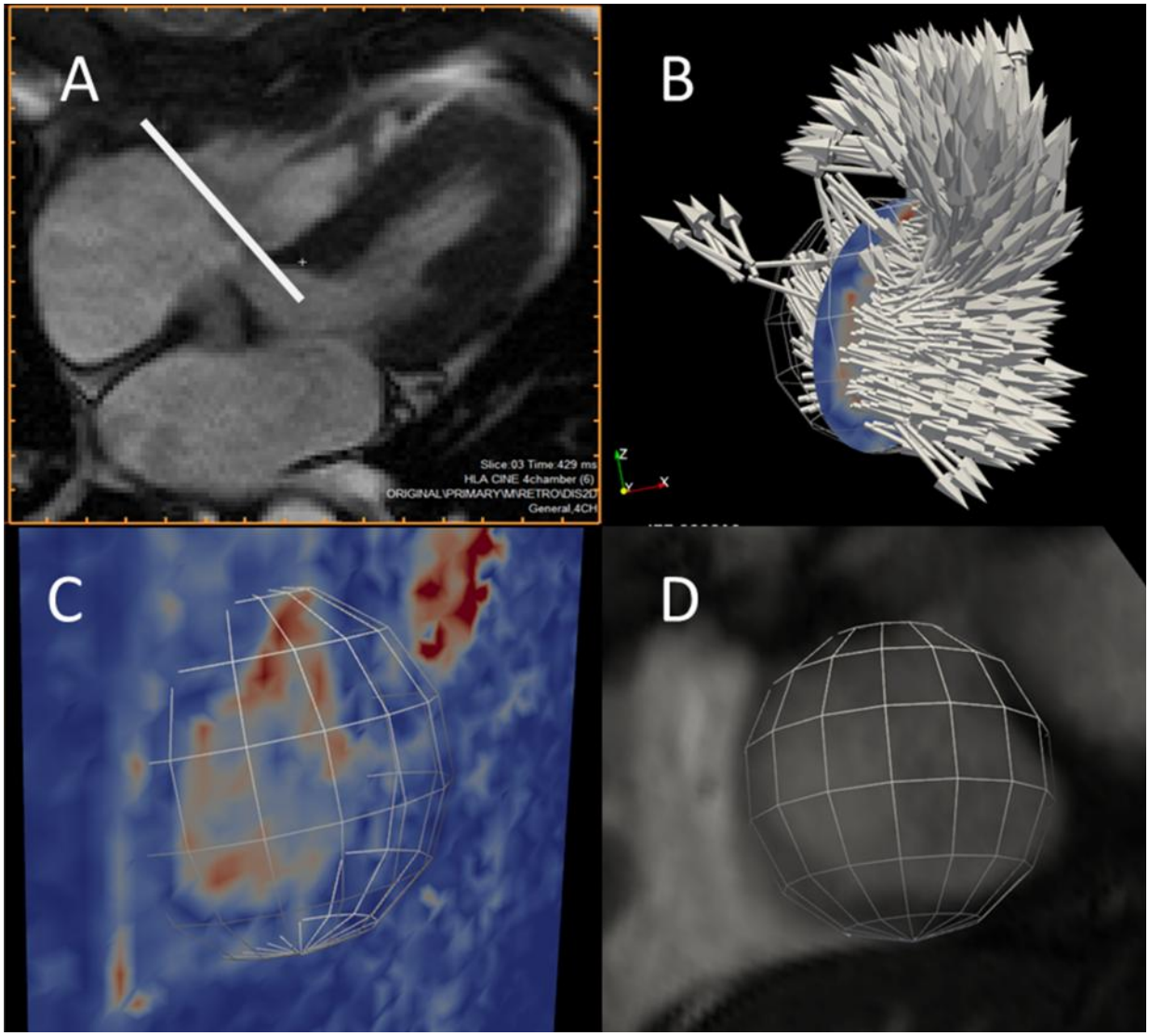

Figure 9. Available data used to locate the diastolic TV plane and circular area. A) 4-chamber cine tissue contrast image at early diastole with a line denoting the TV plane. B) Velocity vectors at early diastole in the region of the tricuspid valve showing the disk location. C) a plane colored by velocity magnitude at early diastole showing the spherical clip used to produce the disk. D) A short-axis tissue contrast cine image showing the TV blood pool at early diastole.

A plane roughly perpendicular to the MPA was located for each subject in a region between the pulmonary valve and the left/right split using axial cine images. An initial location found in which spatial separation between the MPA and Aorta during systole was large enough to prevent aortic flow from contaminating the MPA velocity data. A similar method to TV flow was then used to refine the size and

location of a disk over which normal velocity was integrated over the disk to produce a time series of MPA flowrate (see Figure 10)

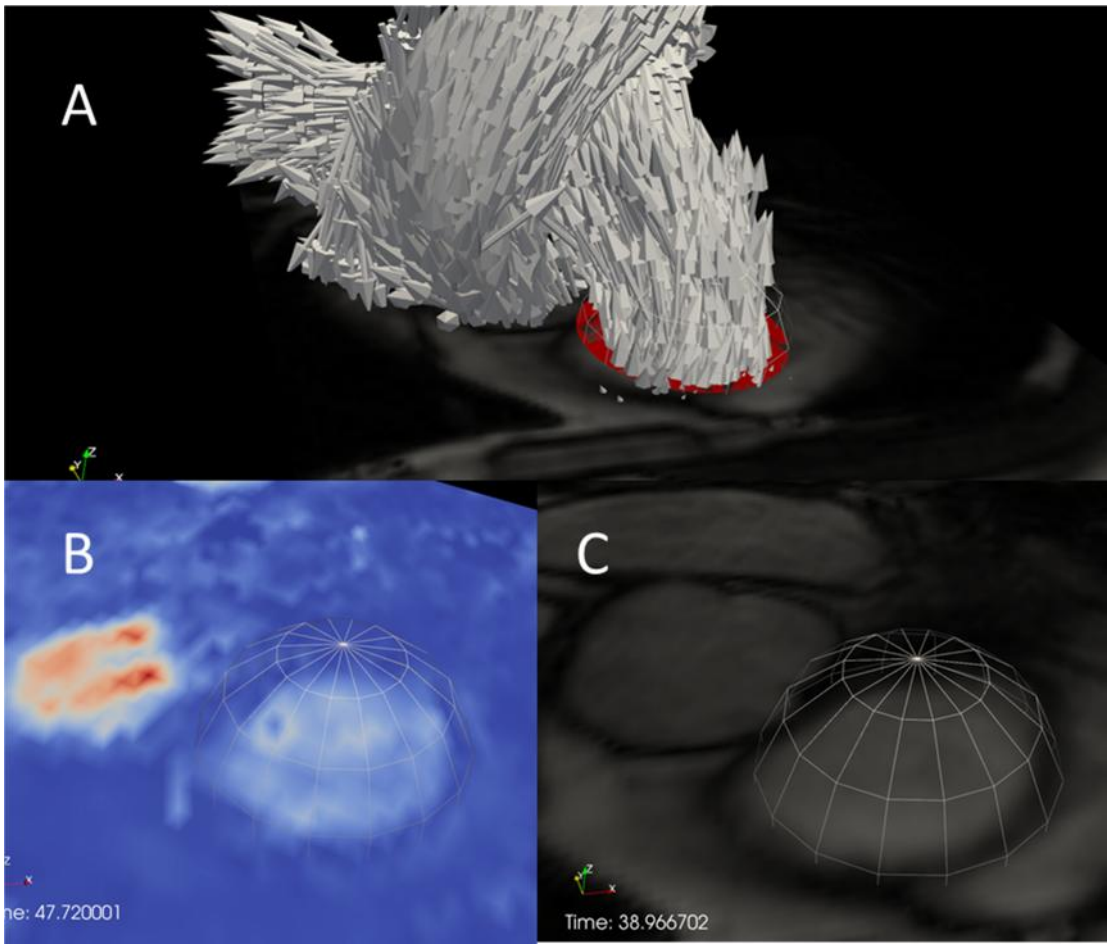

Figure 10. Data used in locating a disk in the MPA for MPA flowrate calculations. A) An axial tissue contrast cine image with velocity vector glyphs and the disk colored in red during systole. Note the proximity of MPA and Aortic vertical flow. B) A slice of velocity data colored by velocity magnitude showing the spherical clip. C) An axial tissue contrast cine image showing the spherical clip.

4.4. Segmentation and LV Volume Curves

A velocity sum of squares (VSS) PC-MRA segmentation workflow was developed which uses the Velomap software package (Bock et al. 2007) in conjunction with a custom connected-set algorithm. The Velomap VSS algorithm calculates the sum of squares over all time steps for each pixel of noise filtered data, and applies a lower threshold to the resulting data to isolate regions of blood flow from static tissue. A novel connected-set algorithm was then developed to further isolate the cardiac regions of interest from unconnected regions to produce a cleaner segmentation and clearer visualization of cardiac structures. The connected-set algorithm builds a non-directional graph from the 3D VSS data, with pixels represented as nodes and an edge between two nodes of they are spatially adjacent and both exceed a user defined VSS threshold value. A non-directed graph representation of the connected-set method is shown in Figure 11

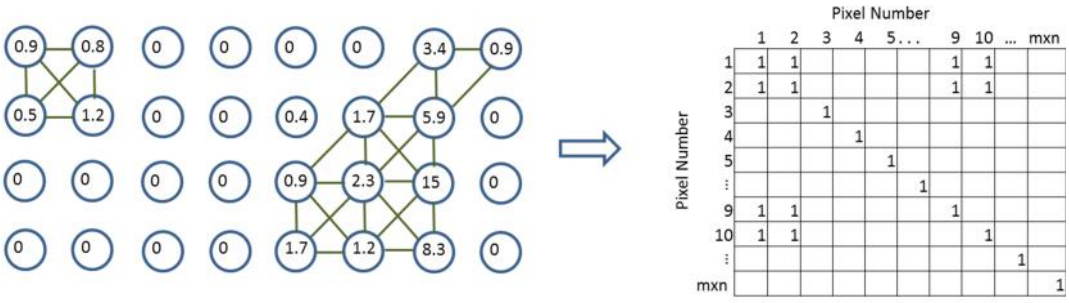

Figure 11. A non-directional graph representation of image pixels showing edges and nodes.

The left ventricular endocardium of each subject was semi-automatically segmented at each short-axis cine image time step using the research version of Medviso's Segment software, v1.9 R3763 (Heiberg et al. 2005). The slice most proximal to the mitral valve included in the segmentation was that which did not include aortic volume at any time step - in most cases this is the second or third most proximal slice in the series. The last apical slice used was the slice that contained LV volume at the end of systole. Each

segmentation boundary curve was visually inspected for accuracy, and in rare cases in which the curve differed considerably from the visible endocardium, the curves were manually corrected in Segment. LV segmentation curves at the beginning and end of systole for a representative subject are shown in Figure 12. The resulting LV volume time-series were exported for each subject and the center-averaged time derivative of volume for each subject was calculated at all time steps. Forward difference and backward difference was used for the first and last time steps respectively. Figure 13 shows LV volume and dV/dt time series from a representative normal subject. For this subject, the dV/dt curve shows well defined peak systolic, early diastolic, and late diastolic times at 134 ms, 534 ms, and 1024 ms respectively.

In addition to semi-automatic LV segmentation, manual segmentation was performed for the RA and RV for one normal and one RVDD subject. These segmentations, executed for the purposes of visualization, were performed within Segment using a manual trace in short-axis, axial, and 4-chamber image planes at all timesteps allowing for a full 3D mask of the RV and RA walls.

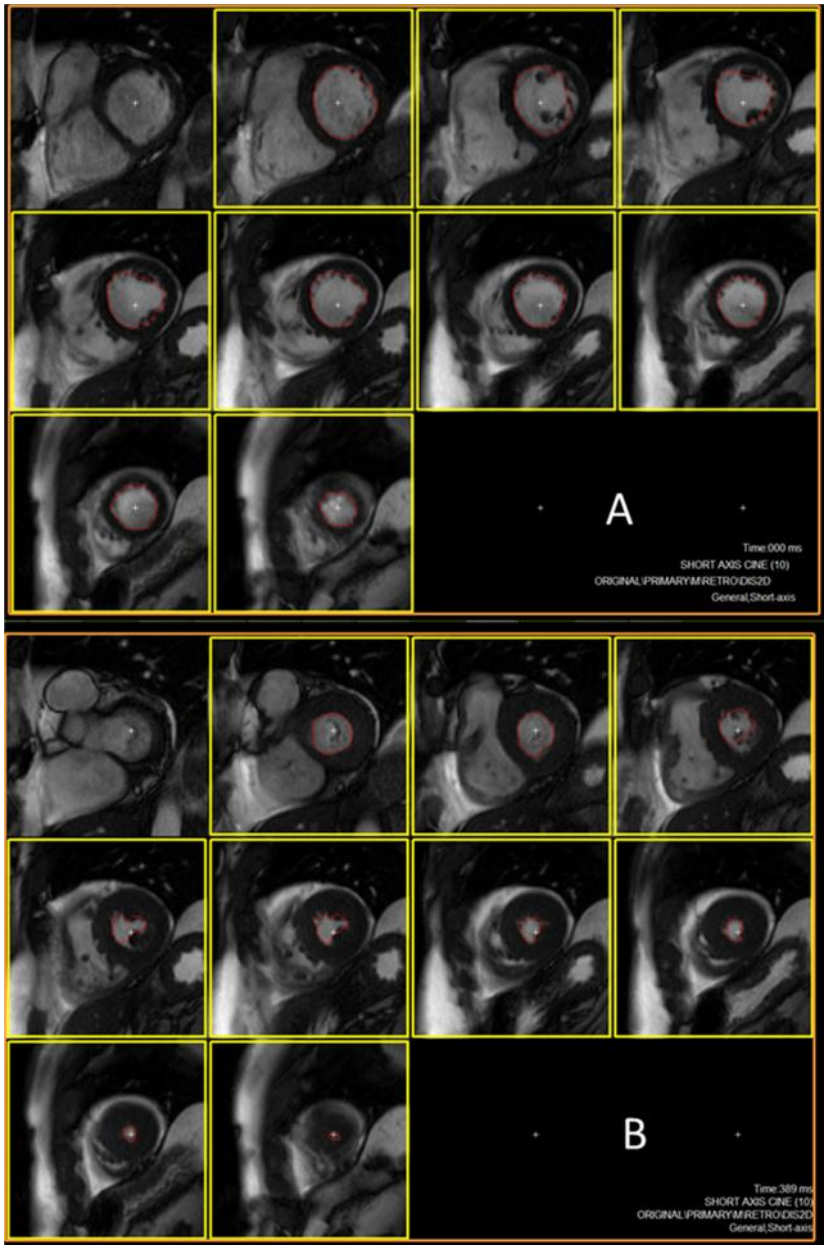

Figure 12. Short-axis automatic left ventricle segmentation curves at A) beginning of systole, and B) beginning of diastole. Note that the first slice is not segmented due to aortic volume intruding in the image at the beginning of diastole.

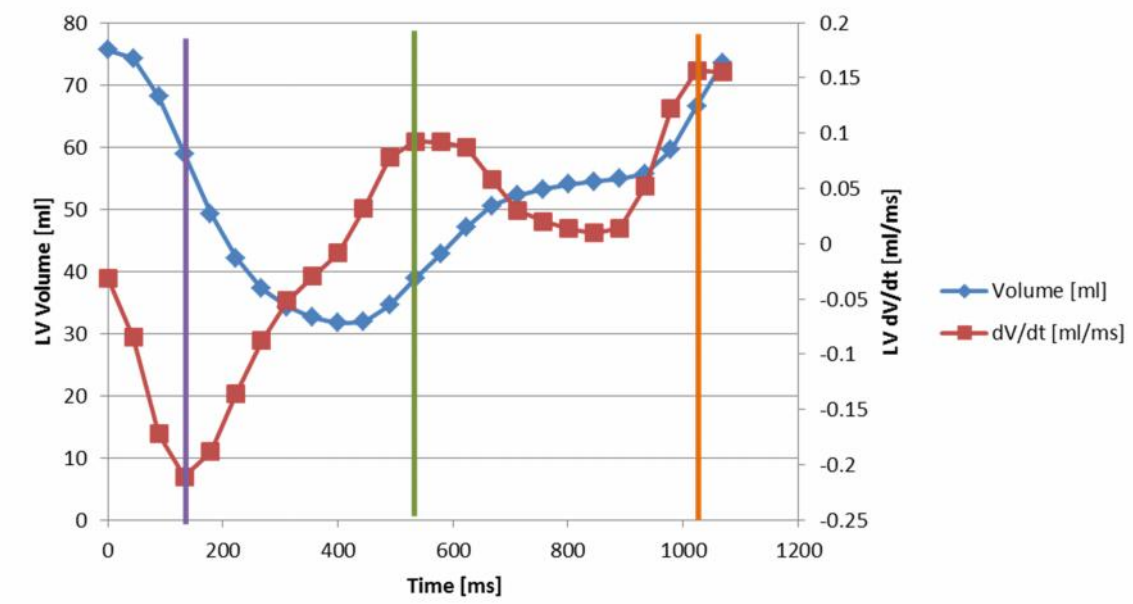

Figure 13. LV volume (diamond markers) and dV/dt (square markers) time series from a representative normal subject.

4.5. Defining Right Heart Regions of Interest

The combined RA + RV volume was manually isolated using a rectangular prism oriented along the RA/RV longitudinal axis using early diastolic vorticity vectors and 2D short-axis and 4-chamber CMR images as a visual guide (see Figure 14). The rectangular prism was oriented such that RH diastolic vorticity vectors were included in the volume, while any vorticity in the LV and ascending aorta was excluded. A subjective judgment was often made regarding the location of the inferior and superior vena cava – which may have a significant effect on the results, particularly in patients with diastolic backflow in the vena cava for which significant diastolic vorticity was present in the veins. In order to separate the RV from the RA, the early diastolic 4-chamber tissue contrast image is used to assist in locating the tricuspid plane.

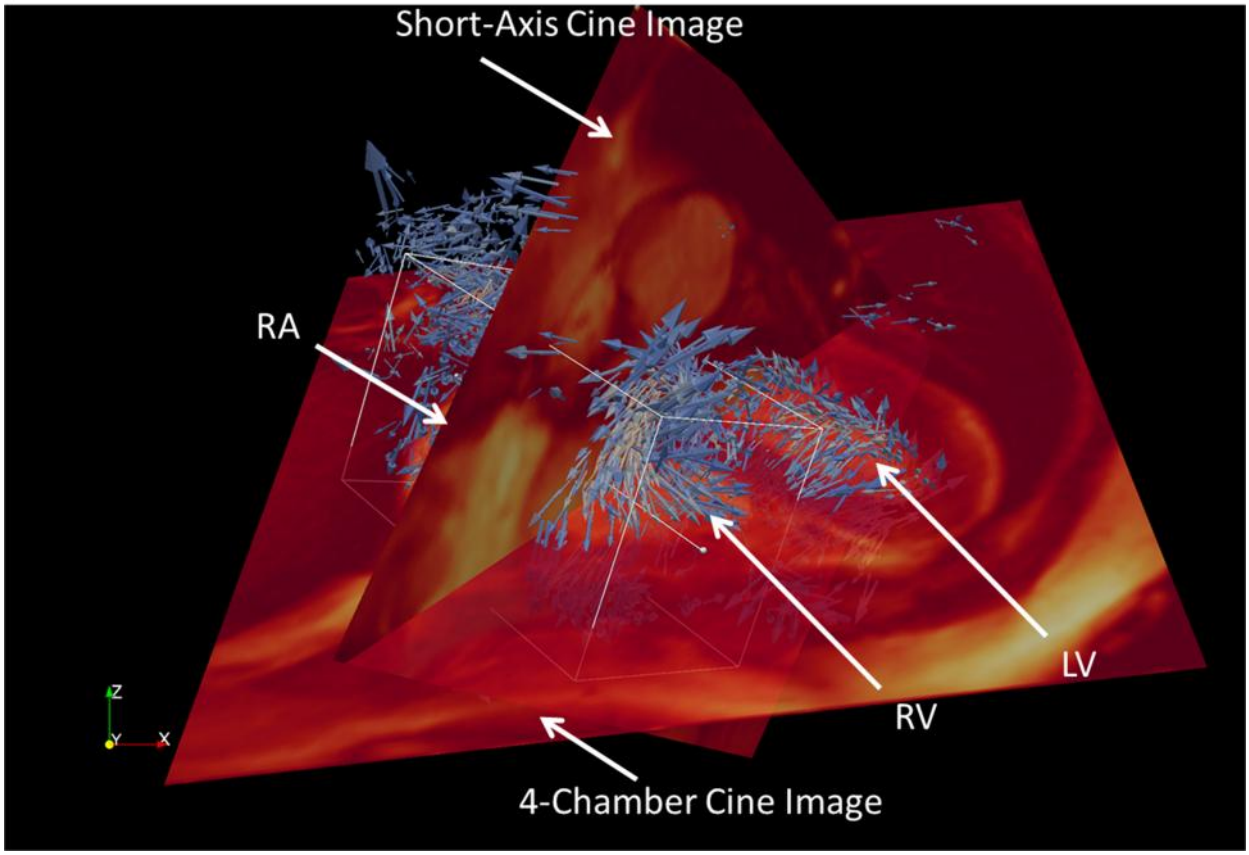

Figure 14. Vorticity vectors in an RV volume during early diastole in a healthy subject. The cuboid encloses the RV volume used for volumetric vorticity integration.

4.6. Calculating Vorticity

Vorticity Thresholding

Isolating the RA, RV, or RA+RV volumes using a rectangular prism allows for an influence on the resulting vorticity integration of contributions from small regions of velocity that may lie outside the physical boundaries of the right heart chambers. These velocities may be due to blood vessels, velocity noise in tissue regions, or tissue motion. Both these velocities and associated vorticity levels were low, so in order to reduce the sensitivity of the results on the subjective placement of the rectangular prismatic region of interest, small vorticity vectors were removed from the ROI prior to volume integration by setting all vorticity magnitudes below a threshold value to zero. This resulted in integration of the large

vorticity vectors only, and a vorticity-free buffer region near the prismatic surface walls. Thus small changes in surface placement have minimal effect on the integration, and numerical problems with partial cell integrations are avoided. Vorticity thresholding involved deciding on a vorticity magnitude threshold level for a single healthy subject, and then scaling that value for the remainder of the subjects using a cardiac flow parameter. Cardiac index (CI) was ultimately used as a vorticity threshold scaling parameter due to its incorporation of several parameters including heart rate, stroke volume, and body surface area. By scaling the threshold value to CI, the effect of body size and the flowrate of the heart are minimized, resulting in a larger inter-subject effect due to changes in flow structures. The threshold value was chosen which improved interobserver reliability while increasing the effect size of RVDD on E-wave vorticity. Details are described below.

In addition to the aforementioned CI scaled thresholding, vorticity was also thresholded at constant levels across all subjects in order to determine the impact on the results of the choice of scaling parameter. Interobserver reliability was investigated using the constant thresholding for a 23 subject subset of the cohort.

Vorticity integration and scaling

The resulting thresholded vorticity element summations were multiplied by voxel volume to get the spatial integration of vorticity. Integrated vorticity was then scaled by CI to again reduce the dependency of the results on body mass, heart size, and heart rate; factors that are expected to influence overall vorticity, but which are not closely related to cardiac pathology. The resulting scaled and spatially integrated vorticity was then used as our metric of interest.

Interobserver reliability

Right heart vorticity at peak E-wave was calculated by two trained analysts using the method previously described for an initial 23 subject cohort consisting of 13 RVDD patients and 10 controls. The concordance correlation coefficient was calculated between the two analysts' results for several threshold levels ranging from .005 to 0.100 s^{-1} .005 s^{-1} increments in order to examine the effect of threshold level on interobserver reliability.

4.7. Quantifying Q-Criterion and Lambda$_2$

Q-criterion and Lambda$_2$ was calculated within ParaView for each pixel within the identical rectangular prismatic RH and RV volumes used for vorticity analysis. Q-criterion was calculated using the ParaView Gradient of Unstructured DataSet filter which contains a Q-criterion option. A python script was written to calculate the Lambda$_2$ criterion within a ParaView Programmable Filter. The script is shown in Appendix A. Q-criterion and Lambda$_2$ values within the RH and RV volumes were exported for all 4DMRI timesteps for each subject and the resulting count of pixels matching each criterion were multiplied by voxel volume resulting in a total volume for each subject meeting the criteria ($\lambda_2 < 0$ or $Q > 0$). T-tests between RVDD and normal groups were calculated for both straight volumes and volumes scaled by cine derived end diastolic volumes (RVEDV).

5. Results

5.1. Preliminary Results

A study of early and late diastolic right heart vorticity was performed on an initial subset of the full cohort which included all Siemens subjects (see Table 2). In addition to vorticity, results for the VSS segmentation technique as well as a visualization of early diastolic vorticity in in the tricuspid plane are presented. These preliminary results were used to guide methodology for the larger study of the full cohort.

VSS Segmentation

The VSS/connected-set segmentation was found to be effective for isolation of the major arteries and veins, including the ascending and descending aorta, the MPA, and the inferior vena cava. However, this method was not successful for segmentation of the right and left ventricles or atria. Figure 15 shows a visualization of a VSS segmentation (left) and VSS segmentation with the novel connected-set algorithm (right). Both images show good segmentation of the major arteries and veins with the connected-set algorithm decreasing extraneous structures. The regions of the heart chambers are not resolved and present as a semi-opaque mass without clearly defined boundaries.

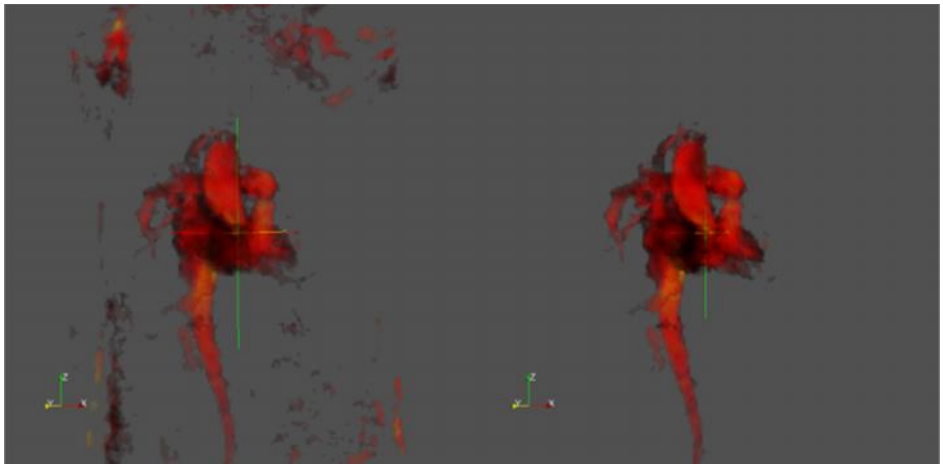

Figure 15. 3D visualization of VSS (left) and VSS with connected-set (right) segmentations. The connected-set algorithm cleans up the image improving visualization particularly when the image is rotated in a 3D viewer.

Preliminary Techniques for Analysis of Diastolic Vorticity

A preliminary workflow, similar to that described in sections 4.5 and 4.6 was developed for integrating vorticity in the RA, RV and RA+RV volumes for all resolved timesteps in a 4DMRI scan using ParaView software . The cardiac region of interest (RA, RV, or RA+RV volumes) are isolated using a rectangular prism oriented along the RA/RV longitudinal axis using early and late diastolic velocity and vorticity vectors as a visual guide (See Figure 16). An early diastolic 4-chamber tissue contrast image is used to assist in locating the tricuspid plane separating the RA from the RV. Before spatially integrating the vorticity vectors in the three regions of interest, vorticity vectors were thresholded to remove regions of low magnitude vorticity from the integral as described in section 4.6.. Threshold values were scaled for each subject based on cardiac index, with a baseline of 0.055 1/s chosen for a healthy subject.

The integral of vorticity magnitude over the RA, RV and RA+RV volumes was calculated at each timestep using the cumulative sum function in ParaView's calculator, with the resulting sum multiplied by voxel volume. These values were then divided by cardiac index since vorticity scales with velocity gradients which in turn are expected to scale with CI.

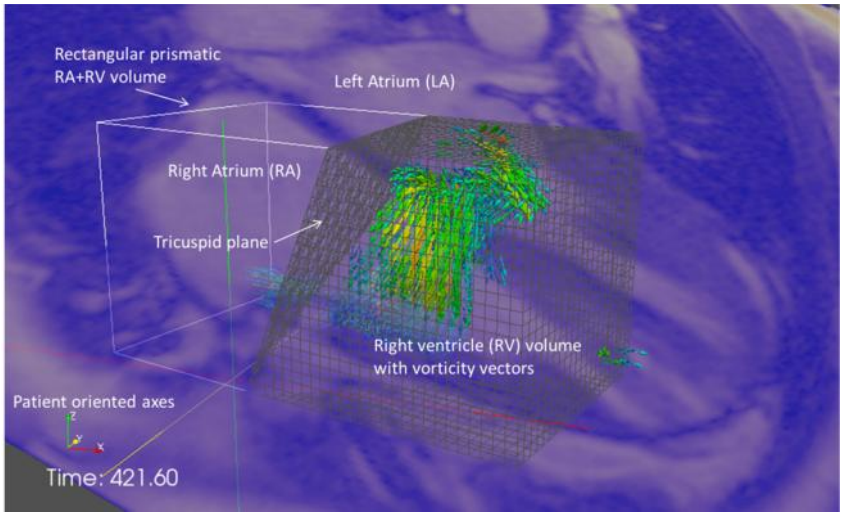

Figure 16. Vorticity vectors in an RV volume during early diastole. The mesh surfaces enclose the RV volume used for volumetric vorticity integration.

Preliminary Qualitative Analysis Techniques

Preliminary techniques and workflows for visualizing coherent right heart flow patterns in ParaView were developed which allowed for qualitative analysis of right heart flow characteristics. The most useful techniques for qualitative analysis were the use of streamlines, velocity vectors and vorticity vectors. Semi-transparent high resolution tissue contrast images enhance these analyses by making it easier to locate cardiac anatomical features in 3D space. Streamlines, vorticity vectors, and cine tissue contrast images were combined to give a clear sense of flow in the RV and the extent of the RV diastolic ring as shown in Figure 17.

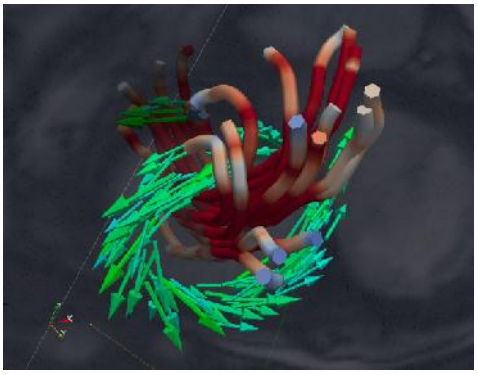

Figure 17. Visualization of an E-wave ring vortex for control and RVDD subjects viewed from the RV apex toward the TV showing streamlines and vorticity vectors. Flow enters the RV through the TV forming a wall generated vortex ring before curling up towards the RV outflow tract.

Right Heart Vorticity in Subjects with RVDD – Preliminary Results

Using the aforementioned techniques, a preliminary study was undertaken to examine quantitative and qualitative differences between subjects with RVDD+PAH and healthy controls.

The study cohort consisted of 13 subjects with right heart catheterization proven PAH and 10 age-matched controls. Each subject had same-day echocardiography and cardiac 4DMRI scans. Echocardiography was used to assess left and right ventricle parameters including E-wave and A-wave RV and LV filling velocities and e' tissue velocities for both the mitral and tricuspid valve. PAH subjects were diagnosed as stage I (TV E/A < .8, TV E/e' > 6, and DT > 120 ms) or stage II (TV E/A = 0.8-2.1, E/e' > 6, and DT > 120 ms) RVDD based on echocardiographic parameters (Rudski et al. 2010). Quantitatively, we found that RVDD was associated with decreased integrated E wave vorticity in both the RV ($1.25 \times 10^7 \pm 1.40 \times 10^7$ mm^2 vs. $3.86 \times 10^7 \pm 2.23 \times 10^7$ mm^2, $p = 0.0012$) and the RA ($2.90 \times 10^7 \pm 2.28 \times 10^7$ mm^2 vs. $4.52 \times 10^6 \pm 3.75 \times 10^6$ mm^2, $p = 0.0005$) (See figure 12). RV and RA integrated vorticity also correlated significantly with RV diastolic echocardiographic markers including TV e' velocity, A-wave velocity, and E/A ratio, and LV markers including mitral valve e' velocity, A-wave velocity, and mitral valve E/A ratio.

The fact that E-wave vorticity correlated with both RV and LV diastolic markers suggests ventricular interdependency in the RVDD+PAH pathology.

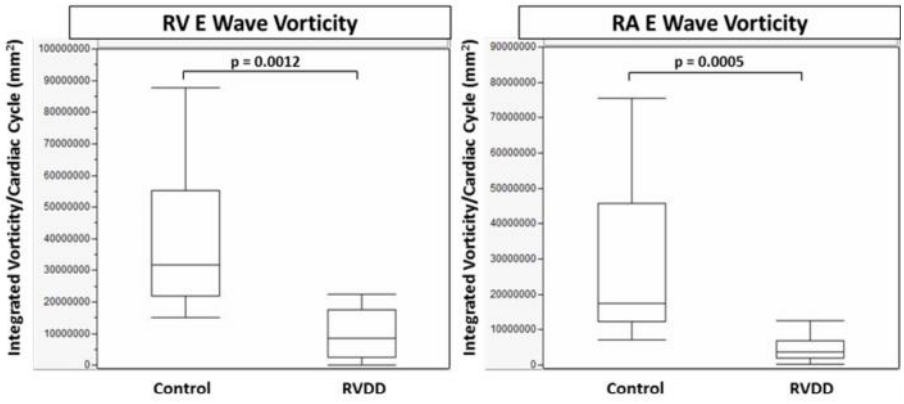

Figure 18. Median RV and RA E wave vorticity in controls vs. RVDD groups. Box plots display the distribution of data including the minimum (bottom whisker), first quartile (bottom of rectangle), median (middle segment), third quartile (top of rectangle), and maximum (top whisker).

Figure 13 is a view of E-wave streamlines and vorticity vectors looking from the RV apex though the tricuspid plane and towards the RA for 21 RVDD and normal subjects from this study. Vorticity vectors have been thresholded as described in section 3.2 and are colored by vorticity magnitude. Velocity streamlines are colored by velocity magnitude. Although normal (blue background) and stage I RVDD (tan background) subjects appear to have similar levels of vorticity contained in the TV/RV vortex ring, stage II RVDD (green background) subjects appear to have significantly less vorticity in the TV/RV vortex ring, indicating that the reduced E-wave vorticity correlation with the RVDD group is driven largely by reduced vorticity in the Stage II RVDD group.

In this initial study, decreased volume-integrated E-wave vorticity was found in a group of thirteen RVDD subjects compared to ten age-matched controls. E-wave vorticity correlated with both RV and LV diastolic markers suggesting ventricular interdependency. 4DMRI was found to be a useful non-invasive

technique for studying right heart coherent flow structures, and has potential for clinical non-invasive diagnosis and monitoring of RVDD.

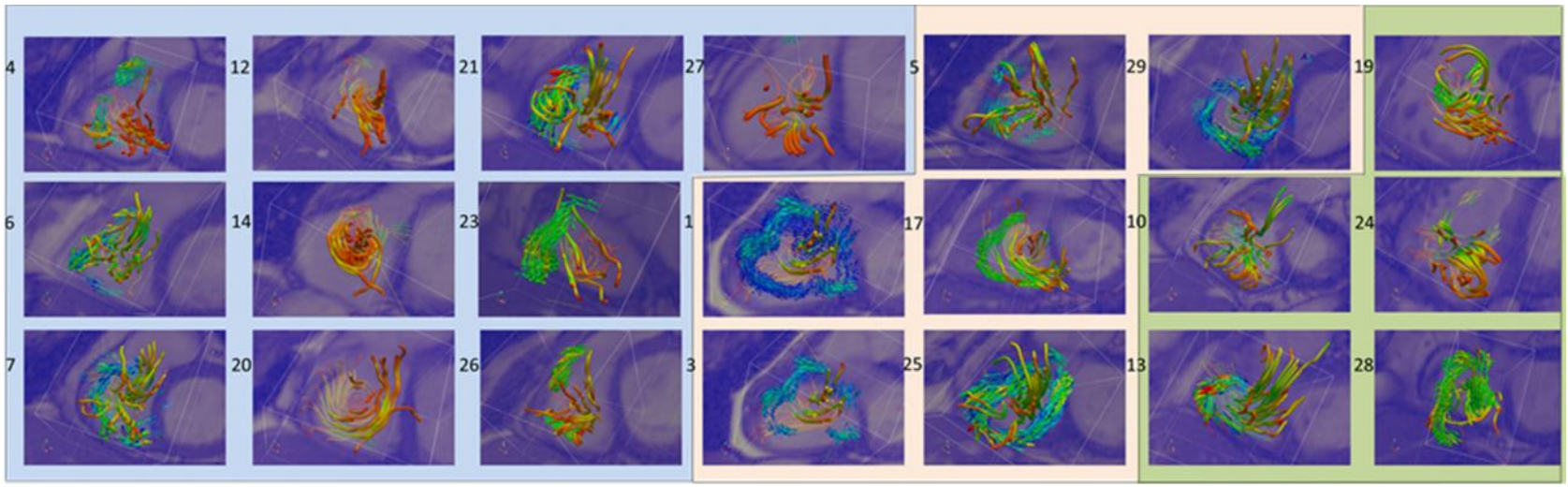

Figure 19. Visualizations of E wave ring vortex for control and RVDD subjects viewed from the RV apex toward the TV showing streamlines and vorticity vectors. Moving from left to right in the image, the subjects go from healthy (blue background), Stage I RVDD (tan background), and Stage II RVDD (green background). Vorticity vectors have been thresholded as described in section 3.2. Each case is identified by an acquisition identification number.

5.2. 4DMRI Data Characteristics

Several relevant properties of the 4DMRI and cine data sets were characterized including spatial and temporal resolution, variation in nominal interval (related to heart rate) within and between data types, and data truncation at the beginning and end of the cardiac cycle. Temporal resolution impacts the ability to accurately measure flow properties at the peak time of cardiac events, while data truncation potentially impacts data quality at peak late diastole.

Spatial and Temporal Resolutions and Variation in Nominal Interval

All 4DMRI velocity images had constant temporal resolution of 50 ms. Spatial resolution for these images varied depending on the volume of the scan region. Slice thickness for all scans was 3mm, however in-plane resolution varied from 1.98-2.60 mm. In general, cine images were both higher spatial and higher temporal resolution than 4DMRI velocity scans. Slice thickness for all cine orientations used in this study (Axial, 4Chamber, and Short-Axis) were 6 mm. Spatial resolution within the image plane ranged from 1.09 – 1.56 mm or roughly twice the linear resolution of 4DMRI images. Temporal resolution ranged from 18-53 ms while the number of timesteps along the cardiac cycle was either 25 or 30. Resolution statistics for cine images are shown in Table 3. Spatial coregistration between 4DMRI and cine data was not measured, but minor coregistration issues are suspected from visual analysis of velocity data and cardiac chamber segmentations from cine data.

Table 3. Spatial and temporal resolution statistics for cine images

	CINE Images				
	Slice Thickness [mm]	Pixel Spacing [mm]	Voxel Volume [mm^2]	Number of Cardiac Images [-]	Time Resolution [ms]
Maximum	6	1.56	14.6	30	53
Minimum	6	1.09	7.2	25	18

For an individual subject, nominal interval was found to vary significantly within a single cine image orientation and between cine images and 4DMRI. The largest range for nominal interval within a single cine series was 38.3% of the mean – occurring for a short-axis image series in which Nominal Interval ranged from 850-1199 ms with a mean of 910 ms. The average range for all cine images was 8.88% of their respective means. The largest magnitude of percentage difference between average short axis cine nominal interval and corresponding 4DMRI nominal interval was 10.7% (4DMRI NI = 994 ms, cine NI = 627 ms) while the absolute minimum was -7.08% (4DMRI NI = 1057 ms, cine NI = 1138 ms).

Data Truncation in Beginning Systole and Peak Late Diastole

The 4DMRI velocity sequence used in this study prescribed prospective gating for 4DMRI phase contrast images, and retrospective gating for cine images. Prospective gating times image acquisition times forward from the QRS trigger while retrospective gating times the image acquisitions backwards from the QRS trigger. Although prospective gating accurately times the first several images in the cardiac cycle, primarily during systole, it can potentially miss the end of late diastole, particularly with a time resolution of 50 ms. Retrospective gating, particularly with a higher time resolution as is the case with the cine images used in this study, is more likely to capture the end of late diastole. Visual inspection of diastolic TV flowrate curves from velocity data, together with left ventricle dV/dt curves produced from cine data (see section 4.3), indicated that late diastolic data may be truncated in the 4DMRI velocity data sets, but not in the cine data. Shown in Figure 20 are TV and MPA flowrate and LV dV/dt curves for a normal subject. Note that the late diastolic region of the LV curve, produced from cine data, shows a distinct peak, whereas the late diastolic region through the TV indicates an acceleration of blood but no distinct peak or indication of deceleration.

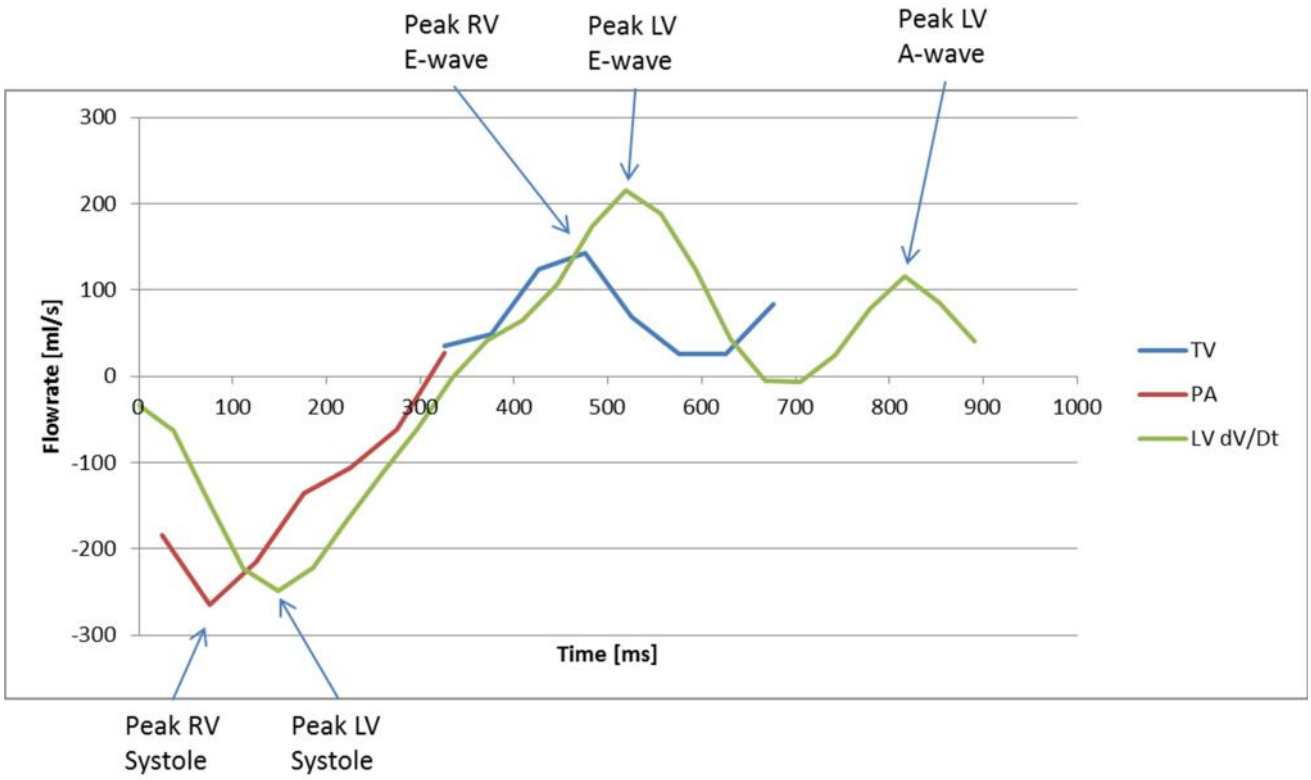

Figure 20. TV and MPA flowrates and time derivative of LV volume for a normal subject suspected of 4DMRI velocity data truncation.

In order to characterize the inaccuracies that may be present due to 4DMRI data truncation, the total flow through the MPA during systole was compared to the total diastolic flow through the TV for all subjects via trapezoidal integration of the TV and MPA flowrate curves. Assuming no MPA or TV regurgitation, the two integrals should be equal within the limitations of the 50 ms spatial resolution of the velocity data in this study. For the entire cohort, we found an average 5.0% deficit in TV flow compared to MPA flow indicating a systematic truncation of late diastolic data. Interestingly, for the normal group, this increased to an average 21.8% deficit of TV flow compared to MPA flow, while the RVDD group had a 7.3% surplus. One explanation for this difference between the RVDD and normal groups may be a prevalence of TV regurgitation in RVDD subjects which would lower integrated MPA flow. Tricuspid valve regurgitation may be more prevalent in the RVDD group due to increase RH

pressures leading to cardiomyopathy which causes abnormal closing of the TV leaflets. Regardless of the cause of these inconsistencies between TV and MPA time integrated flowrates, the results of this data analysis, together with visual inspection of the late diastolic regions of subject TV flowrate curves, have not allowed for accurate analysis of late diastolic hemodynamics.

5.3. Cardiac Segmentation

Cardiac segmentation was performed for two primary reasons. One is to provide LV volume curves for LV/RV synchronicity analysis presented in section 5.4 and the second is for the purposes of flow visualization presented in section 5.6. As described in section 4.4, automatic segmentation of the left ventricle is currently a more established technique than segmentation of the LA, RA, or RV due to the irregular morphology of these three heart chambers. Figure 21 shows a time-resolved semi-automatic left ventricle segmentation using short-axis cine images and Medivso Segment software. Note that from end diastole to end systole, the LV apex shifts towards the mitral valve resulting in a difficulty of segmenting the end diastolic LV apex using the same image planes throughout the cardiac cycle. Also shown for reference is a temporally co-registered semi-opaque 4-chamber image. Both the LV epicardium and endocardium surfaces from the segmentation match the location of the epicardium and endocardium in the 4-chamber image. Note that the ventricular contraction that occurs between end diastole and end systole results in a large contraction of the endocardial surface, a relatively smaller contraction of the epicardium surface, and a resulting thickening of the heart muscle.

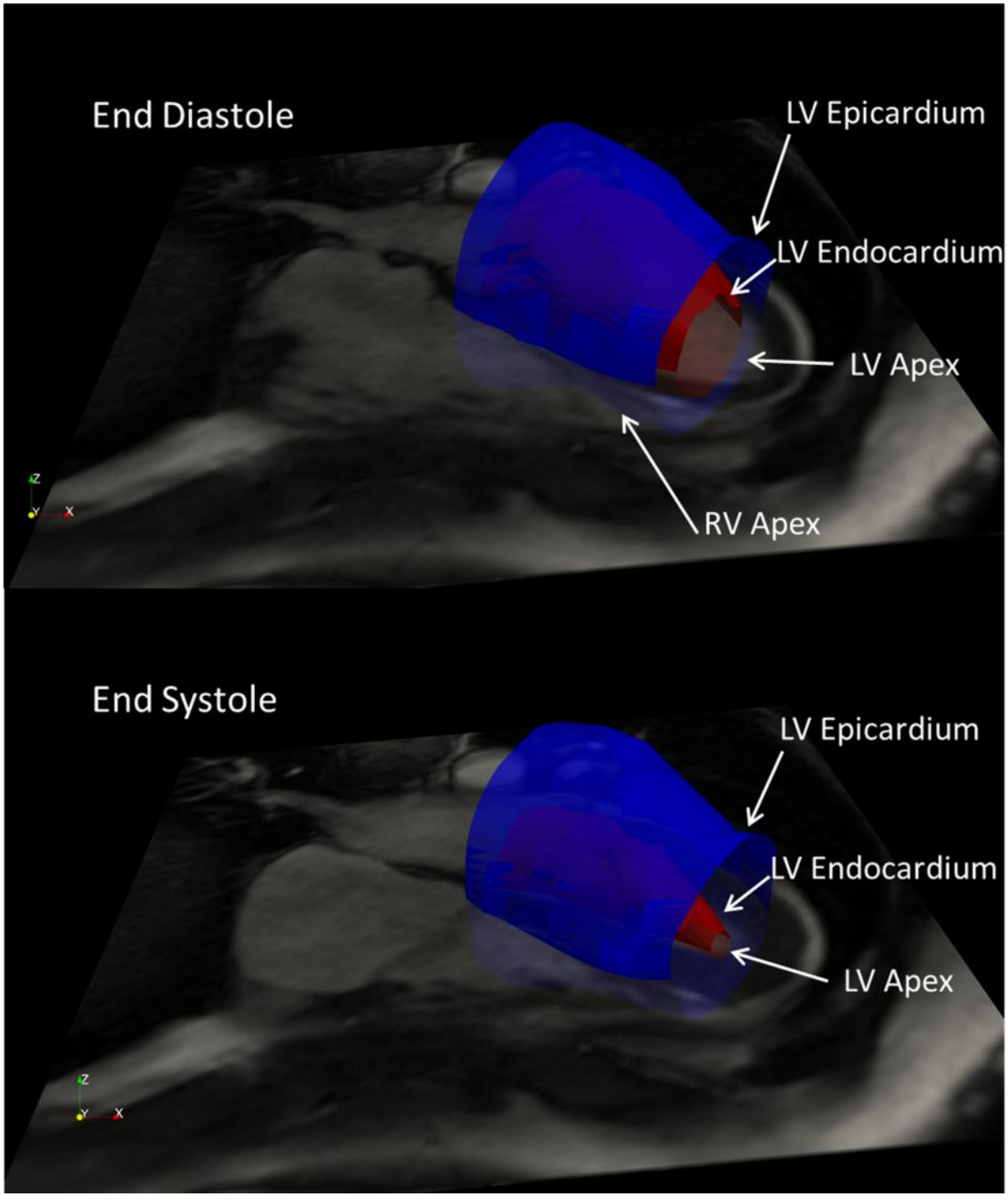

Figure 21. Left ventricle segmentation for a healthy subject during the end of diastole and end sytole.

Manual RA and RV segmentations were performed using Medviso Segment using 4-chamber images for a normal subject and short-axis and axial images for an RVDD subject. Figure 22 shows the results of the 4-chamber endocardium segmentation at peak diastole including velocity vectors and a 4-chamber slice for reference. The segmentations show good spatial matching between the RV (purple) and RA (green) due to the ease of tracing the TV boundary between the two chambers using a 4-chamber image. However, because the 4-chamber image stack does not cover the entirety of the z-axis length of the RA and RV volumes, several important details of the RH physiology are not included in the segmentation including the RV outflow tract, the IVC and SVC inflow. Compared to the short-axis LV segmentation shown in Figure 21, the 4-chameber method does a better job of accurately segmenting the RV apex. Figure 23 shows a time-resolved RV endocardium segmentation using short-axis cine images and an RA segmentation using axial cine images. Compared to the 4-chamber RV segmentation, the short-axis RV segmentation (purple) includes more of the right ventricle outflow tract. However, the interface between the RA and RV includes a large dislocation due to the most proximal slice of the short-axis cine stack including both outflow tract and TV disk. The axial cine RA segmentation (green) provides improved detail of the IVC and SVC inflow regions in of the RA. A clear problem with the RA axial cine segmentation is the TV region where velocity vectors appear to move through the RA epicardium wall towards the RV inflow. This is due to the complex geometry of the RA in which the 2D intersection of the RA volume and the axial images morphs into two non-overlapping cross sectional shapes as the axial image is moved from the center of the RA towards the caudad (foot) direction. Similarly, the intersection of the RV volume and the short-axis image plane morphs into two shapes – the TV plane and the right ventricular outflow tract. Because manual segmentation does not allow for multiple closed traces per image, one of the shapes (in the case of the RA the IVC inflow was chosen) must be chosen.

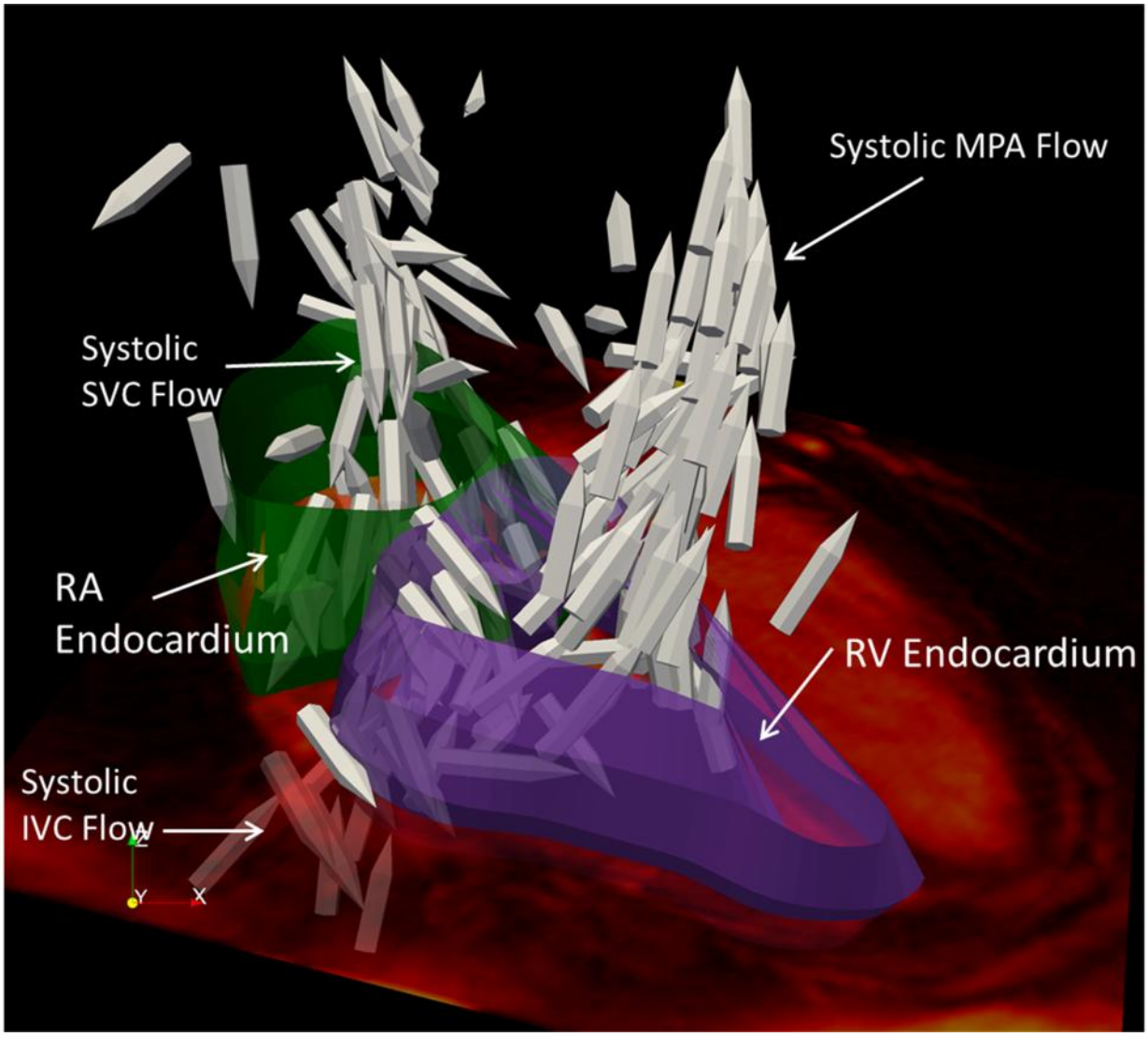

Figure 22. Time-resolved 4-chamber manual RA and RV segmentations during peak systole using 4-chamber cine images for both RA and RV. The RV is shown as a purple surface, and the RA is green. Thresholded Velocity vectors are shown as grey pencil shapes. Shown for reference is a semi-opaque 4-chmaber tissue contrast slice shown in a red scale. The subject is normal.

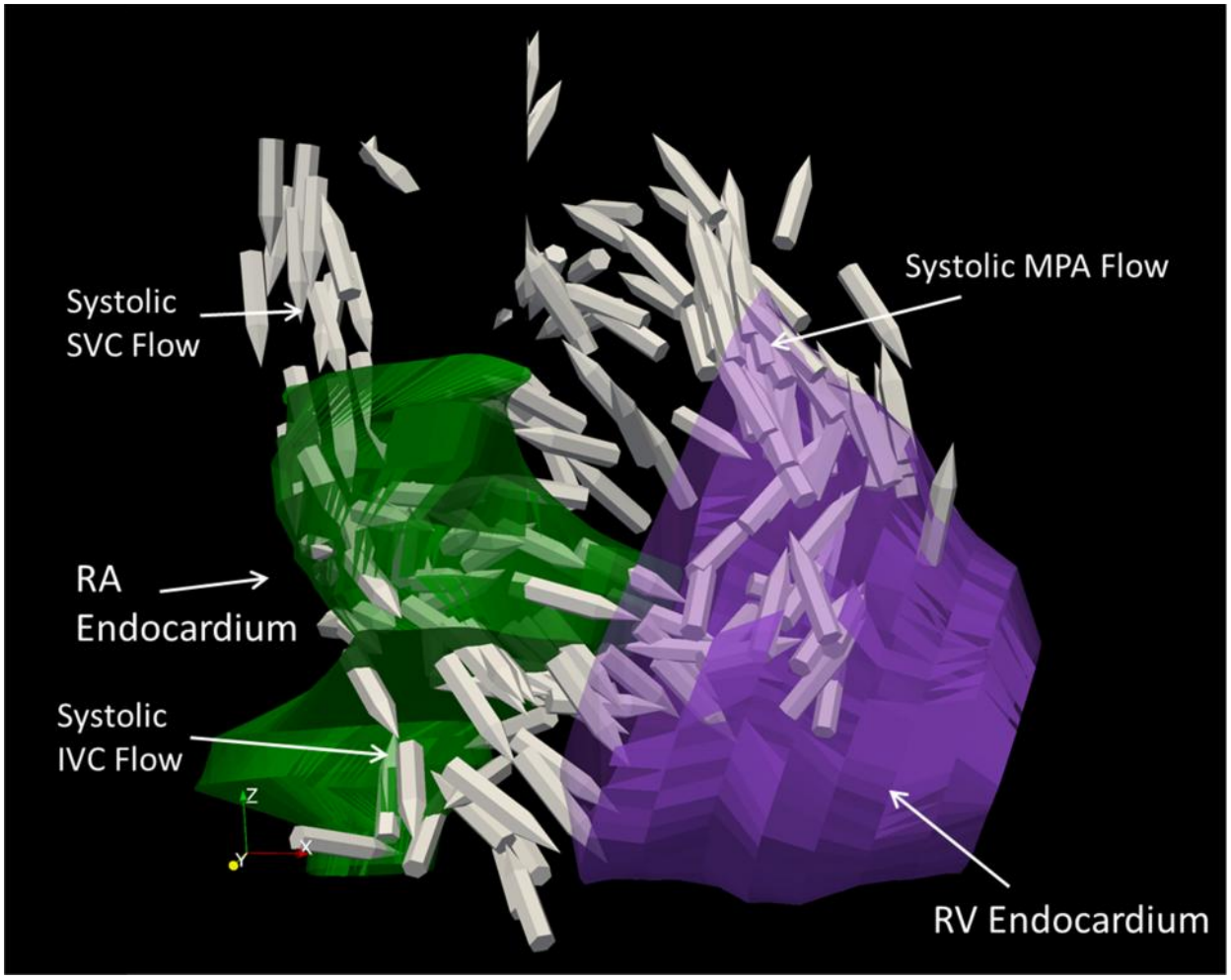

Figure 23. . Time-resolved 4-chamber manual RA and RV segmentations during peak systole using short-axis and axial cine images for the RV and RA respectively. The RV is shown as a purple surface, and the RA is green. Thresholded Velocity vectors are shown as grey pencil shapes. The subject is from the RVDD group.

5.4. Cardiac Event Timing and Right/Left Heart Synchronicity

Several important characteristics of cardiac MRI confound the ability to use 4DMRI and high-res cine data to approximate the timing of cardiac events. The first is the significant change that can occur in a subject's heart rate during the course of scan. For example, during the course of the 4DMRI portion of a scan, a heart rate interval is set within which an acquisition is accepted. However, this may vary considerably from the acceptable heart rate interval for cine acquisition leading to difficulties comparing 4DMRI defined right heart events and cine (i.e. automatic LV segmentation) defined left heart events.

The second difficulty was that the 4DMRI data obtained from the particular scanning sequence used in this study was prospectively gated (acquisitions are timed prospectively from a QRS complex trigger) while the cine data is retrospectively gated. The fourth difficulty is simply the low temporal resolution of the 4DMRI data which is kept at 50 ms as a compromise between data quality and total scan time.

Despite these limitations, the 4DRMI TV and MPA flowrate method was found to be a practical method for estimating peak systolic and early diastolic timing in the left and right ventricles. Figure 24 shows flowrates through the MPA and TV as well as the time derivative of LV volume at discrete timesteps in the cardiac cycle of a normal subject. Peak LV and RV systole and E-wave are clearly visible on the plot. However, due to prospective 4DMRI gating, the TV velocity data is potentially truncated at the end of cardiac cycle and it becomes ambiguous whether the last timestep represents true peak LV A-wave. Note also from the figure that the major cardiac events between the left and right heart correspond well, with the left heart events slightly delayed, roughly 20-50 ms. It is unclear whether this delay is due to variation in heart rate between 4DMRI (the data used for TV and MPA flowrate calculation) and cine (data used for LV volume calculation) data acquisition, or if the delay is caused by prospective gated 4DMRI versus retrospective gated cine acquisition techniques. No subjects in this cohort have been diagnosed with electrical heart blockage which would account for delayed left heart events.

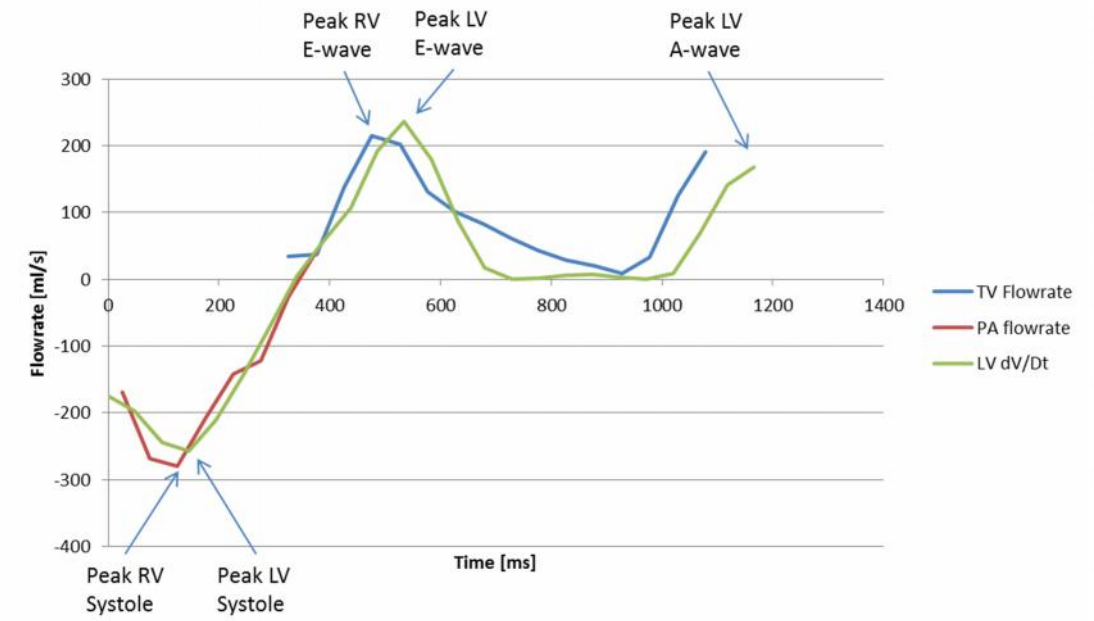

Figure 24. TV and MPA flowrates and time derivative of LV volume for a normal subject

Figure 25 shows flowrate and LV volume curves for a subject with Stage 1 RVDD. In this case, LV A-wave has become dominate over E-wave. Calculating peak E-wave requires examination of the corresponding LV volume curve in order to estimate a time difference between early and late diastole and then work backwards from LV late diastole. Although the E-wave peak is small, it can be seen that a peak does exist at the time that early diastole would be expected. The significant delay in heart events between the left and right heart in this subject is likely due mainly to a decreased HR during the cine portion of the scan (used for LV dV/dT data) versus the 4DMRI portion.

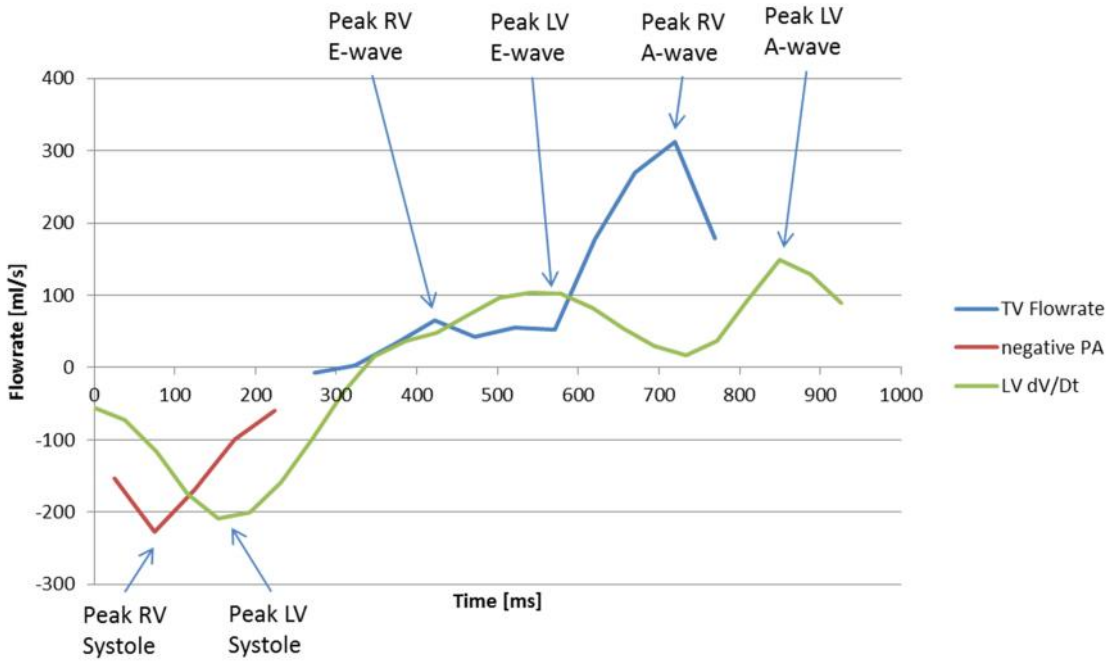

Figure 25. TV and MPA flowrates and time derivative of LV volume for a subject with RVDD

5.5. Peak E wave Vorticity, Q-criterion, and Lambda$_2$

Interobserver reliability

Figure 26 shows concordance coefficient, ρ_c, over a range of vorticity thresholds. The coefficient exceeds 0.90 at a threshold of 0.025 s^{-1} and reached a local peak of 0.922 with a threshold of 0.040 after which little is gained in interobserver reliability with increasing thresholds. Figure 27 shows the effect of increasing threshold on the vorticity vectors in the right heart of normal subject. As the threshold reaches 0.04 s^{-1}, a coherent ring of vorticity resolves through the TV constriction. At 0.05 s^{-2} gaps appear in the ring indicating excessive thresholding and loss of data pertaining to the structure. Based on the threshold images and the concordance coefficient, it appears that 0.04 represents a compromise between excessive data loss and interobserver reliability.

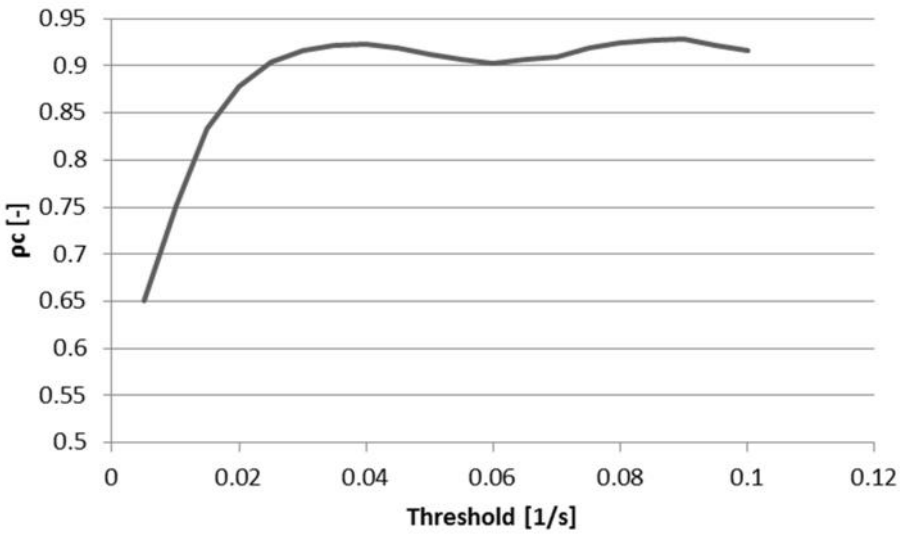

Figure 26. Concordance correlation coefficient of vorticity for two observers at multiple vorticity thresholds

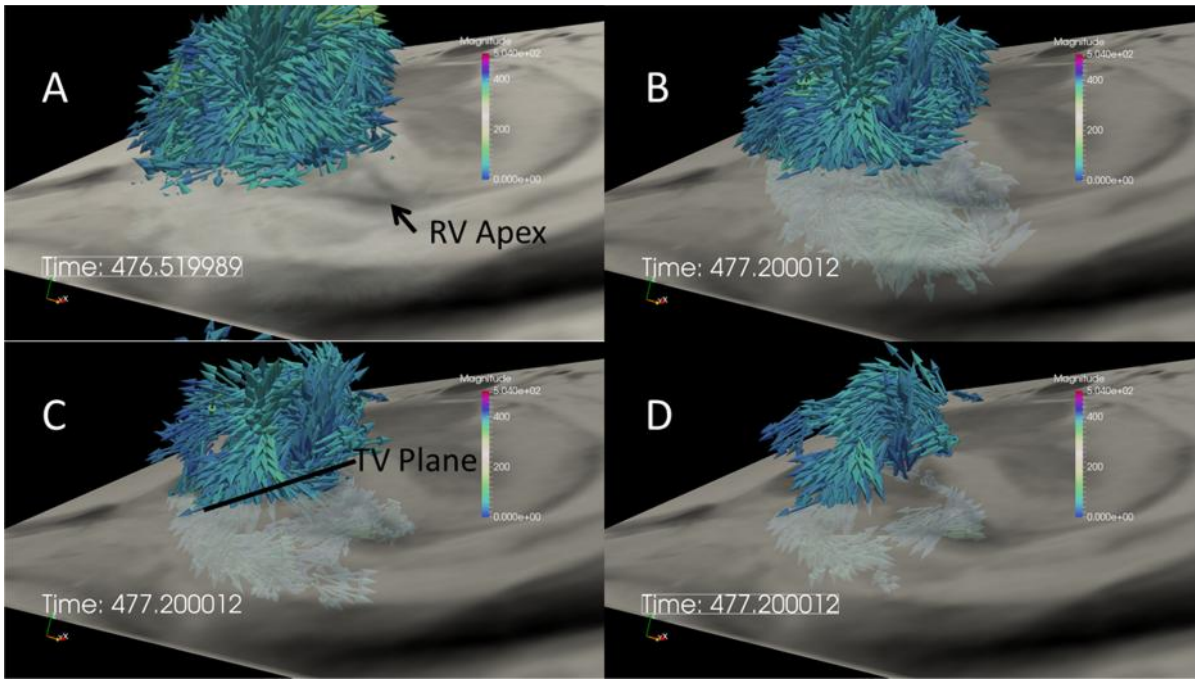

Figure 27. Right heart vorticity during peak early diastole for normal subject thresholded at A) 0.02 s-1, B) 0.02 s-1, C) 0.02 s-1, and D) 0.02 s-1. Vector glyphs are colored by vorticity magnitude and a grayscale 4-Chamber cine image plane is shown for spatial reference.

Peak E-wave Vorticity

Peak early diastolic vorticity in the RV, RA, and RH volumes was integrated within a rectangular prism around the RH using several scaling and thresholding schemes as detailed in the methods section. T-tests were performed to evaluate differences in vorticity between the RVDD group and the normal group for all combinations of thresholding and CI scaling to investigate the effect of these methods on differences between the two groups and to elucidate the optimal technique for potential clinical RVDD diagnostics t-tests between the RVDD and normal groups.

Table 4 shows the results ordered in descending statistical significance for all scaling techniques for which the p-value is less than 0.05. Several trends are evident in the results. First, of the four scaling/thresholding schemes used (no scaling of integrated vorticity plus use of a constant value for thresholding, integrated vorticity scaled by CI, vorticity thresholded by CI scaled values, and a combination of both – None, SS, TS, and SS/TS respectively) the last three methods resulted in significant differences in the populations ($p < 0.05$). With stricter significance definition, only the SS and TS methods resulted in significant differences ($p<0.025$). Second, statistically significant ($p<0.05$) differences between vorticity in the two populations is evident only in the RH and RA regions of interest and not in the RV. With stricter significance ($p<0.025$) they occur exclusively in the RA and are split evenly between the SS and TS scaling methods. Third, 95% statistical significance occurs for a range of threshold values from 0.03 to 0.06, with the more cases occurring with thresholds of 0.03 – 0.05 (0.03 N=4, 0.04 N=4, 0.05 N=4, 0.06 N=3). The highest statistical significant occurred with a right atrial ROI, a constant threshold of 0.04, and with integrated vorticity scaled by CI for which the p-value was 0.014.

Table 4. Results for spatially integrated peak early diastolic vorticity in three regions of interest for several scaling methods. SS = integrated vorticity scaled by cardiac index, TS = vorticity thresholded by cardiac index. Only results showing a p-value of less than 0.05 are shown. P-values increase from left to right. The table is split into two sections due to space limitations.

	p<0.05							
p	0.014	0.016	0.018	0.019	0.021	0.022	0.026	0.028
ROI	RA	RA	RA	RA	RA	RA	RA	RA
Scaling/Threshold Method	SS	TS	TS	SS	TS	SS	TS	SS
Threshold [1/s]	0.04	0.04	0.05	0.05	0.06	0.03	0.03	0.06
Normal Mean Vorticity [L/s]	709	1826	1184	425	750	1121	2685	255
RVDD Mean Vorticity [L/s]	408	1059	602	231	340	730	1833	136

	p<0.05						
p	0.029	0.029	0.032	0.033	0.033	0.039	0.045
ROI	RA	RA	RH	RH	RA	RA	RH
Scaling/Threshold Method	SS/TS	SS/TS	SS/TS	SS/TS	SS/TS	SS/TS	SS/TS
Threshold [1/s]	0.04	0.05	0.04	0.05	0.06	0.03	0.03
Normal Mean Vorticity [L/s]	877	584	1610	1117	377	1251	2265
RVDD Mean Vorticity [L/s]	467	266	949	591	148	796	1531

Q-criterion and Lambda$_2$

The Q-criterion filter and the Lambda$_2$ script were tested on a simulated dataset of a heated rotating plate immersed in fluid. The results, shown in Figure 28, demonstrate that both the lambda$_2$ and the Q-criterion method work as expected – identifying both the toroidal ring vortex above the plate and the line vortex at the plates surface. Also shown are streamlines for the steady-state solution as well as thresholded vorticity vectors. Note that the vorticity vectors show vertical wall shear at the spatial boundary of the solution while not elucidating the toroidal ring vortex or line vortex.

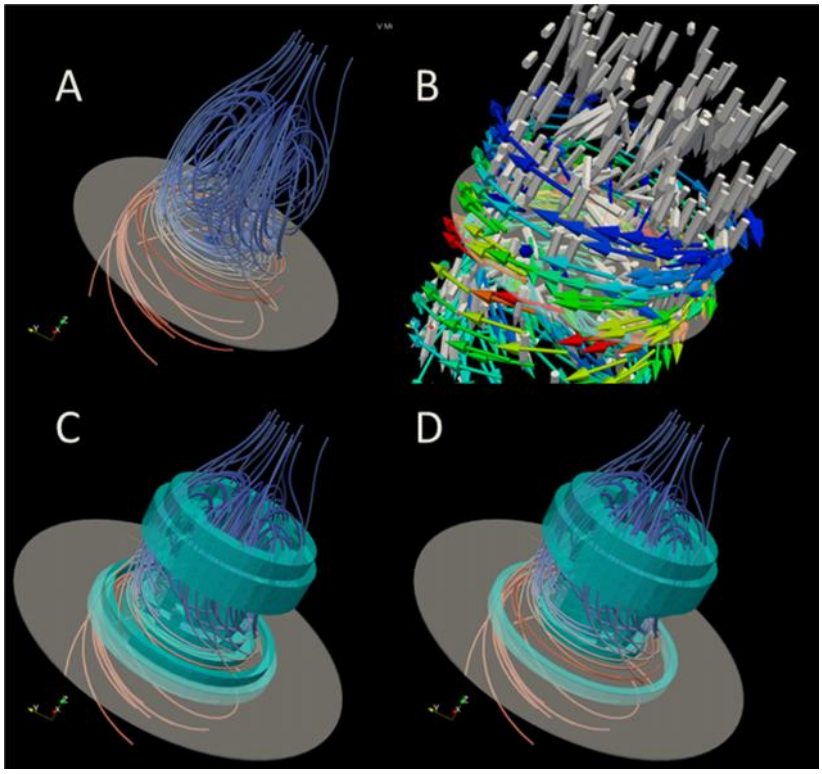

Figure 28. A) Streamlines from immersed heated plate test data set, B) velocity vectors in gray and vorticity vectors colored by vorticity magnitude, C) regions of $\lambda_2<0$, D) Regions of $Q > 0$.

Table 5 shows two-sample, two-tail, unequal variance t-test results for $Lambda_2$ and Q-criterion both scaled by RVEDV and unscaled in the RA, RV, and RH volumes derived using the method described in section 4.7. There is a significantly higher volume (p 0.05) of $Lambda_2$ regions in the right heart during peak early diastole in the RVDD group compared to controls. However, there is not a comparable level of significance in either the RA or RV regions for the unscaled $Lambda_2$ volume. Scaling the resulting volumes of $Lambda_2$ and Q-criterion volumes by RVEDV significantly reduces the difference between the RVDD and normal groups indicating that the difference in RH Q and $Lambda_2$ region volumes are due to larger RVEDV in normals compared to RVDD subjects. In fact, a two-tailed, unequal variance t-test showed significantly higher RVEDV in RVDD subjects versus normals (Normal mean RVEDV = 138 ml, RVDD mean RVEDV = 182 ml, p = 0.022).

Table 5. T-test results for RH Lambda2 and Q-criterion volumes scaled and unscaled.

	$Lambda_2$ Volumes		
	RH	RA	RV
p	0.038	0.150	0.167
Normal Mean [ml]	126	69	56
Normal SE	8.0	5.9	7.7
RVDD Mean [ml]	150	81	69
RVDD SE	7.8	5.4	4.1

	$Lambda_2$ Volumes/RVEDV		
	RH	RA	RV
p	0.715	0.589	0.899
Normal Mean [-]	0.92	0.52	0.41
Normal SE	0.04	0.05	0.05
RVDD Mean [-]	0.90	0.49	0.41
RVDD SE	0.06	0.04	0.03

	Q Volumes		
	RH	RA	RV
p	0.058	0.146	0.075
Normal Mean [ml]	100	56	43
Normal SE	7.4	4.5	3.9
RVDD Mean [ml]	119	66	53
RVDD SE	6.4	4.4	3.7

	Q Volumes/RVEDV		
	RH	RA	RV
p	0.691	0.592	0.997
Normal Mean [-]	0.73	0.42	0.31
Normal SE	0.04	0.03	0.02
RVDD Mean [ml]	0.71	0.39	0.31
RVDD SE	0.04	0.03	0.02

Figure 29 and Figure 30 show peak early diastolic visualizations of $lambda_2$ and Q-criterion results in the right heart for a normal and RVDD subject respectively. In Figure 29a, there are two primary connected regions of blue pixels meeting $lambda_2$ criteria – indicating rotating flow structures. Q-criterion, shown in red in Figure 29b, has similar connected regions as $lambda_s$ but the RA region is smaller. In Figure 29d, the two connected regions have been seeded with forward integrated streamlines to elucidate the structure of rotating flows indicated by $lambda_2$ and Q-criterion analysis. The streamlines indicate a right handed helical flow in the RA and a small line vortex in the region of the posterior leaflet of the tricuspid valve.

Figure 30 shows two views of peak early diastolic $lambda_2$ and Q-criterion regions in the right heart of a subject with RVDD along with velocity vectors and streamlines. In panels A through D, pixels meeting $lambda_2$ (blue) and Q (red) criteria show several connected regions in the RV inflow area just downstream of the TV circumference forming a partial or broken vortex ring. However, the RA helical vortex core present in the normal subject is not present in the RVDD subject. The velocity vectors shown in panel E indicate a flow around the posterior TV leaflet similar to the normal subject. Streamlines shown in panel F, seeded in the center of the RA and the middle of the TV annulus, show substantially

weaker RA helical flow compared to the normal subject as well as further confirmation of flow wrapping around the posterior TV leaflet.

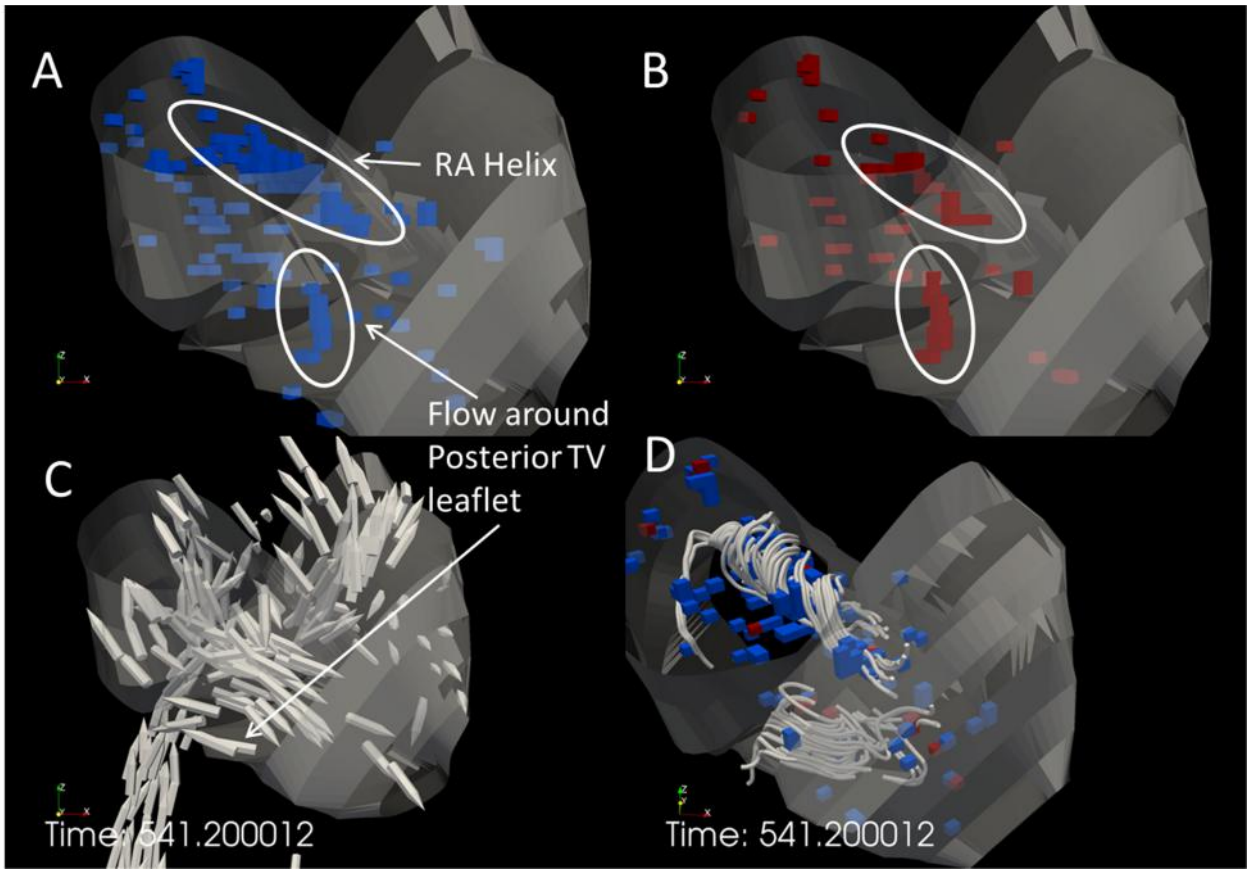

Figure 29. Lambda2 (A), Q-criterion (B), velocity vectors (C), and lambda2, Q-criterion, and two seeded regions of forward integrated streamlines (D) in the right heart for a normal subject at peak early diastole.

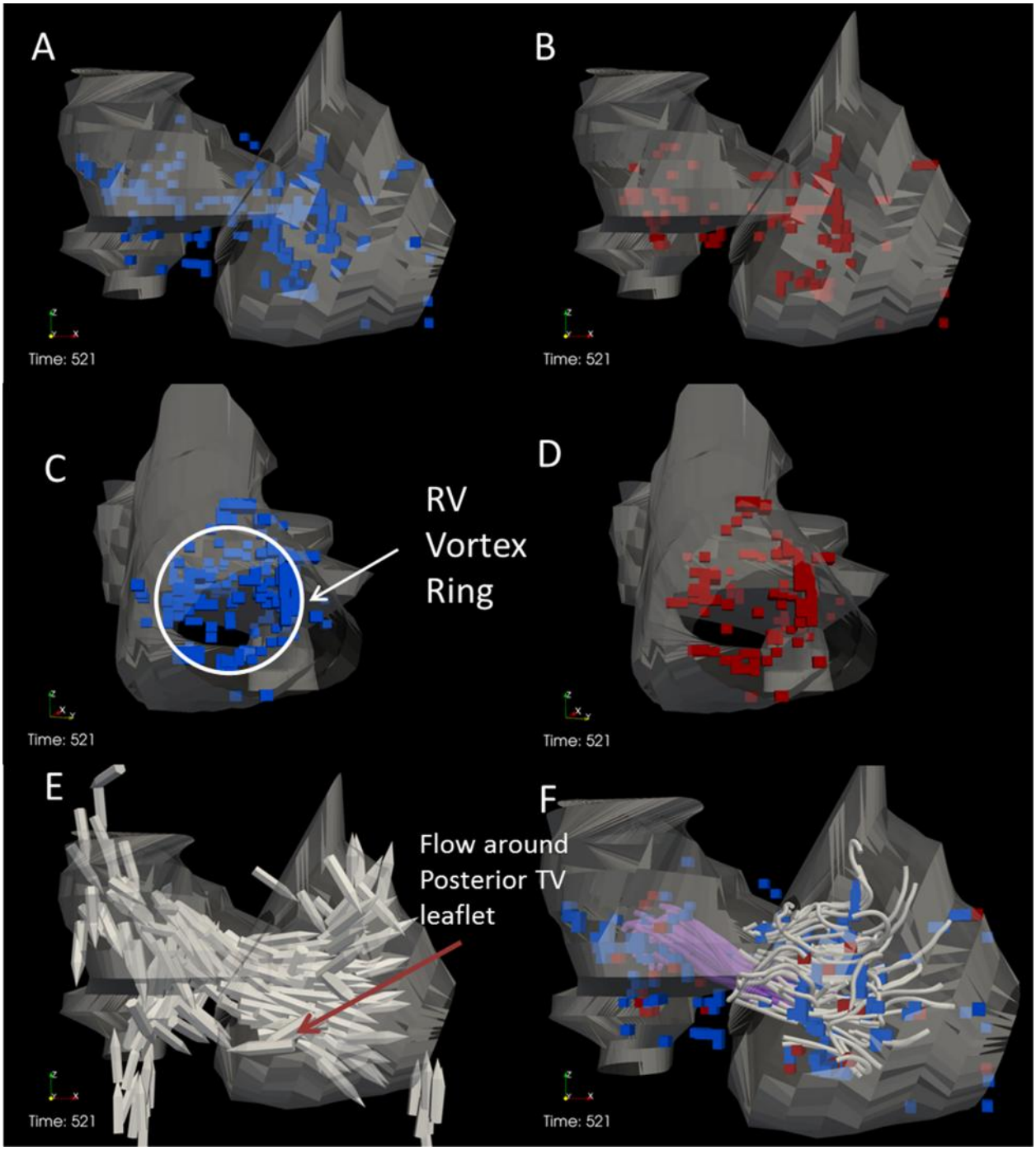

Figure 30. Two views of Lambda2 (A and C), Q-criterion (B and D), velocity vectors (E), and lambda2, Q-criterion, and two seeded regions (RA seed in purple and TV seed in white) of forward integrated streamlines (F) in the right heart of an RVDD subject at peak early diastole.

5.6. Right Heart Flow Visualization

Flow visualizations are presented for an RVDD and normal subject at three timesteps in the cardiac cycle – peak systole, peak early diastole, and late diastole. Though limited to just a single subject from each of the normal and RVDD groups, this analysis attempts a preliminary qualitative characterization of right heart 3D flow in the normal and pathologic state. The subjects were chosen because full RA and RV manual segmentations were available to define boundaries and anatomical locations for flow features, and because both subjects appeared to have minimal late diastolic data truncation which allowed for late diastolic flow characterization.

Normal Cardiac Systolic Flow and Visualization Spatial Orientation

Shown in Figure 31 are four views of flow in the complete cardiac region for a normal subject. Panel A, viewed from patient anterior to posterior direction shows several primary systolic flow features; flow from the RV, through the outflow tract, through the MPA and then split into the right and left pulmonary arteries (rPA and lPA respectively). On the left of the image are the inferior and superior vena cava flows meeting in the right atrium, and the ascending aortic flow leading to the aortic arch. Panel B, rotated 90 degrees in a positive direction about the positive z (superior) patient axis shows a clearer image of the IVC and SVC flows meeting in the RA as well as a clearer view of the descending aorta (Dao). Panel C again shows a clear view of the Dao, and includes a view of the ascending aorta (AsAo) from its origin within the red RV endocardium as well as the rPA wrapping behind the AsAo. Panel D, shown with a semi-transparent LV endocardium and epicardium segmentation shows the MPA stream originating in the LV. Note that in this and subsequent images, velocity and vorticity vectors are lower-thresholded to remove noise and provide a focus on flow structures.

Peak Systolic Flow in a Normal and RVDD Subject

Figure 32 shows peak systolic right heart flow in a normal and RVDD subject. Beginning with the bottom left of panel A, flow from the hepatic vein is seen wrapping clockwise around the main IVC flow stream. At the top left, the SVC stream enters the RA meeting the IVC/Hepatic flow slightly off-center. These three flows combine to form the clockwise helical RA flow in the normal subject described in section 5.5. Although the tricuspid valve - located at the interface between the RV and RA segmentations -is closed, there appears to be velocity vectors pointed towards the RV. This is likely an artifact of tissue motion of the TV annulus which is picked up as velocity by the MRI scanner. High velocity flow through the MPA originates primarily in the center of the RV, but several vectors also originate towards the RV apex. Panel B shows thresholded vorticity vectors in addition to velocity. Vorticity in the right heart during diastole is primarily wall-shear generated vorticity in four regions, the hepatic vein entering the IVC, the IVC, the SVC, and the MPA. Also shown is wall generated vorticity surrounding the ascending aorta. Panels C and D show peak systolic flow in a subject with RVDD. Note that this subject was confirmed to have tricuspid valve regurgitation and an abnormally large right atrium – likely due to high RH pressures coincident with the RVDD and PAH pathology. The flow is similar to that of the normal subject, the main difference being a lack of hepatic flow around the IVC and less vorticity generated in the IVC.

Peak Early Diastolic Flow in a Normal and RVDD Subject

Figure 33 shows peak early diastolic (ventricular relaxation) right heart flow in the normal and RVDD subjects. Blood continues to enter the RA through the inferior and superior vena cava for both subjects with continued mixing of the IVC and SVC streams in the RA. Merging of flow from the hepatic vein into the IVC is no longer visible in the normal subject. The TV is now fully open, and a strong fluid stream moves through the TV annulus in both subjects. However, in the normal subject, the RV inflow clearly splits within the RV with a portion heading upwards through the RVOT and a portion continuing along

the RV long –axis towards the RV apex. In the RVDD subject, this RV inflow split is less well defined. Although not shown in the RV segmentations, the split may be affected by the location shape of the papillary muscles in the ventricles. In the normal subject, significant vorticity continues to be generated at the walls of the IVC, but a new larger region of vorticity is generated in the annulus of the tricuspid valve, with a smaller region of vorticity in the RV apex from the inferior inflow stream split. In the RVDD subject a ring of vorticity is also generated at the TV annulus, but appears to extend further into the RV than in the normal subject. A smaller region of vorticity is in the IVC stream just below the point where it meets the SVC stream in the RA.

Late Diastolic Flow in a Normal and RVDD Subject

Figure 34 shows late diastolic (atrial contraction) right heart flow in the normal and RVDD subjects. In the normal subject, IVC and SVC flow has mostly ceased and a less coherent flow stream is entering the RV through the TV. Vorticity in the normal subject is now generated primarily along the walls of the RA, particularly along the lateral wall. Slight retrograde flow is seen in the IVC due to the atrial contraction. In the RVDD subject, significant retrograde flow is apparent in both the VC and SVC which may be due to increased right heart pressures coincident with the RVDD and PAH pathology. Unlike the normal subject, a large and coherent RV inflow stream is still visible in the RVDD subject due to the dominance of late diastolic RV filling over early diastolic filling that is one of the primary characteristics of the RVDD pathology. In the RVDD subject, a strong region of wall generated vorticity is still seen in the region of the TV annulus, and the RV inflow has now more clearly split into an RVOT stream and a stream which continues towards the RV apex, reminiscent of early diastole in the normal subject.

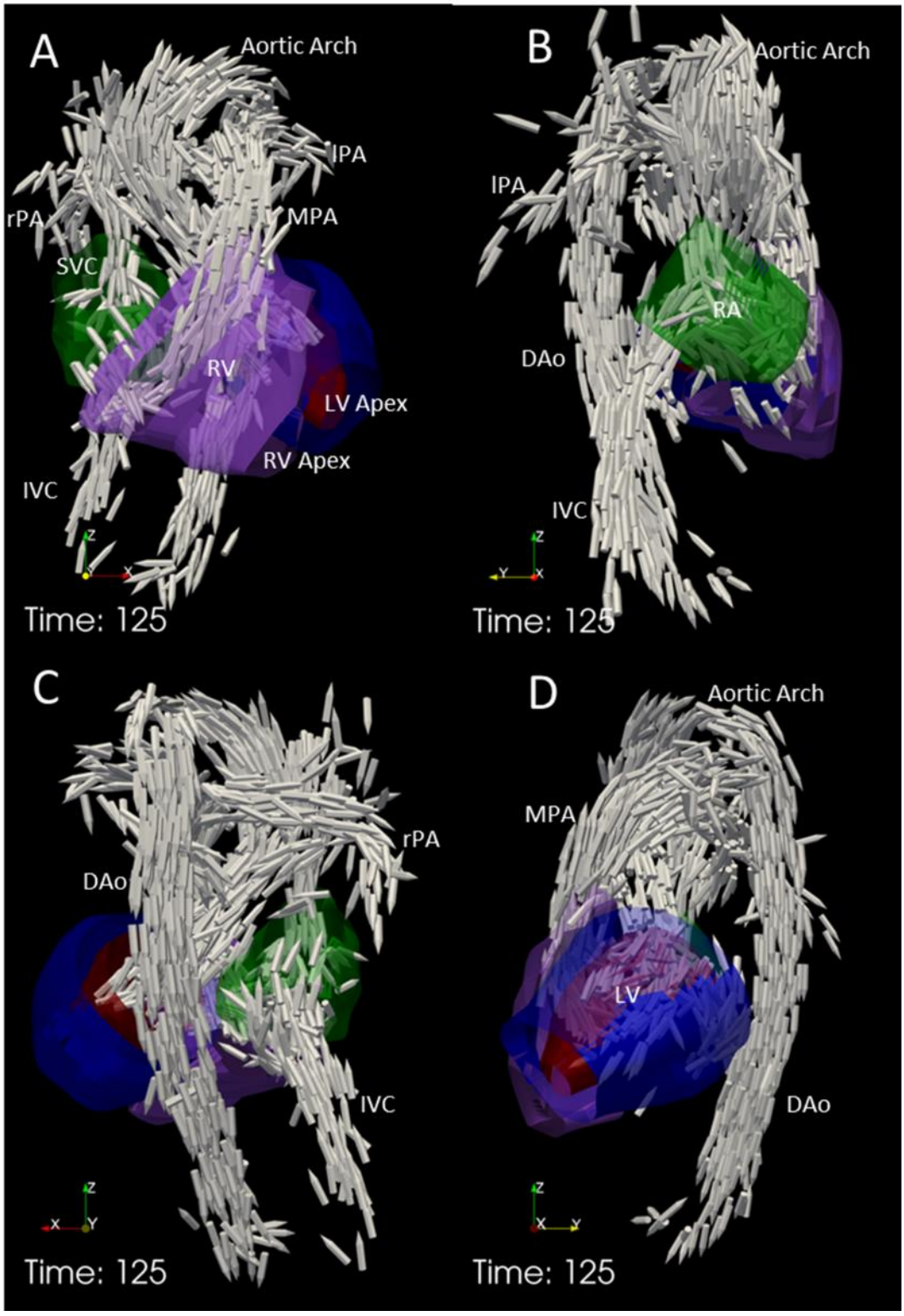

Figure 31. Peak systole in a normal subject. Velocity vectors are shown in white. LV endocardium, LV epicardium, RV, and RA segmentations are shown in red, blue, purple and green respectively. Starting from the top left, the image is rotated 90 degrees in each subsequent image in a positive direction about the patient positive z axis.

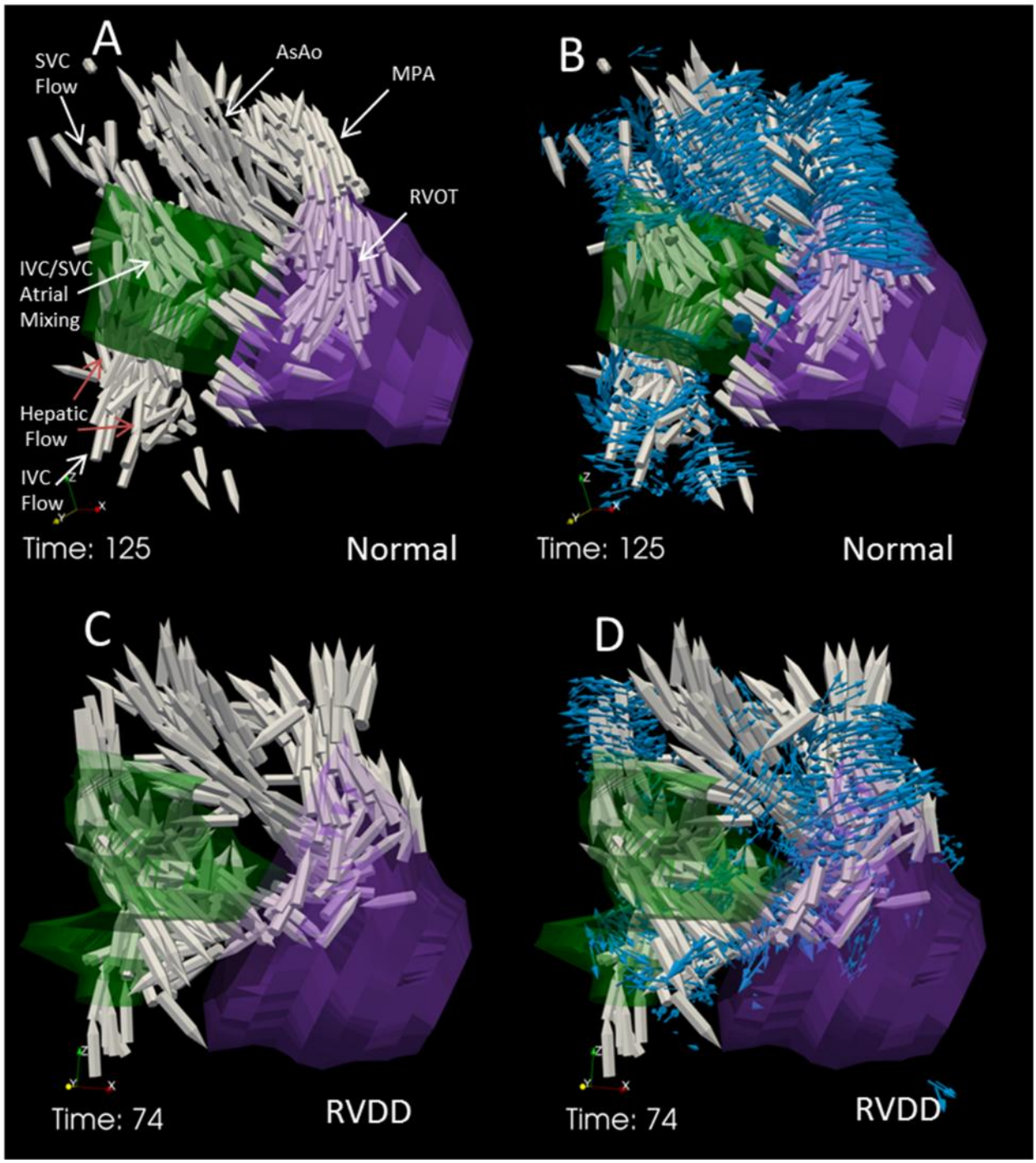

Figure 32. Peak systolic flow visualization in the right heart for a normal and RVDD subject. Velocity vectors are shown in white, vorticity vectors are blue, and RV and RA endocardium segmentations are purple and green respectively.

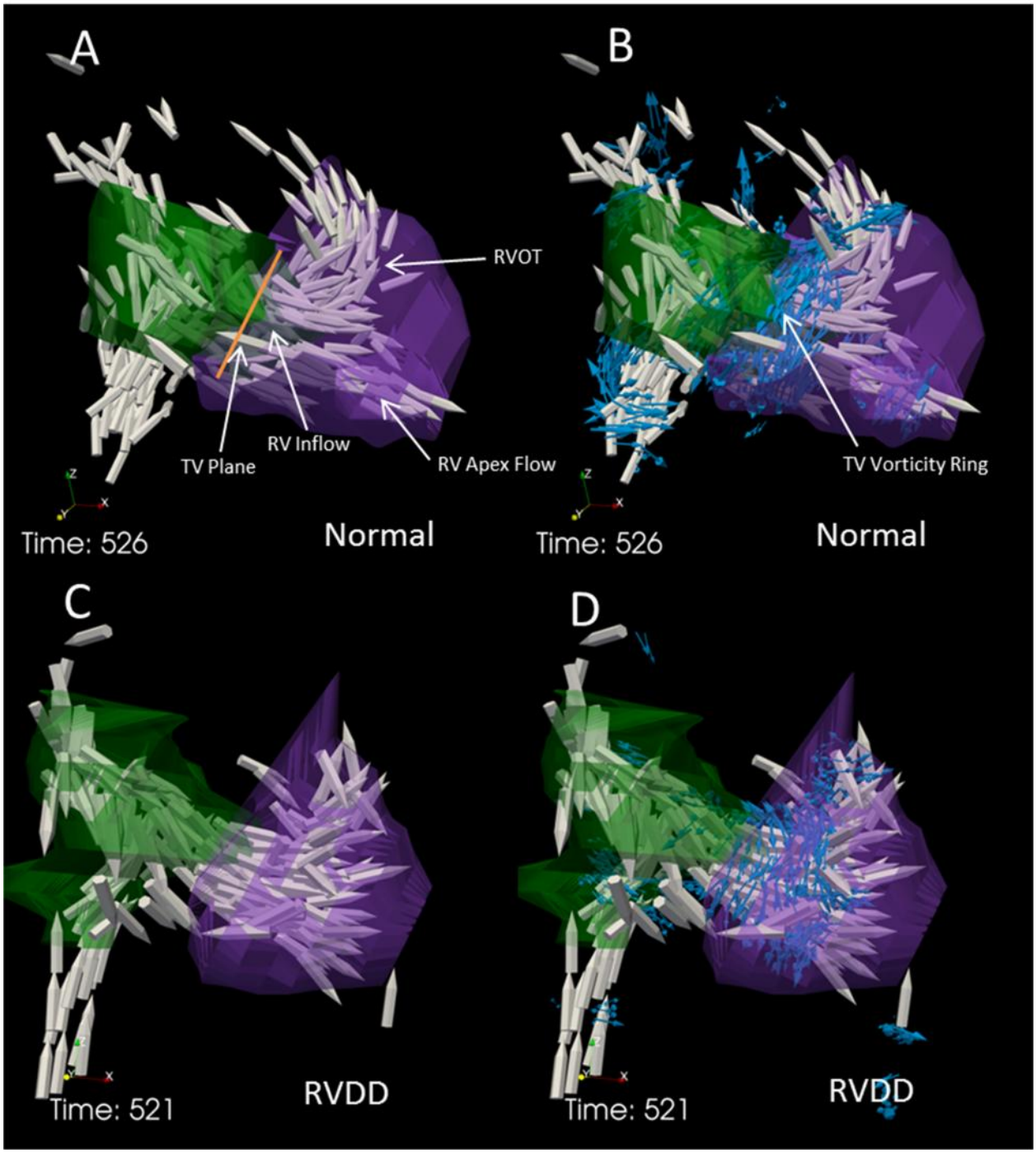

Figure 33. . Peak early diastolic flow visualization in the right heart for a normal and RVDD subject. Velocity vectors are shown in white, vorticity vectors are blue, and RV and RA endocardium segmentations are purple and green respectively.

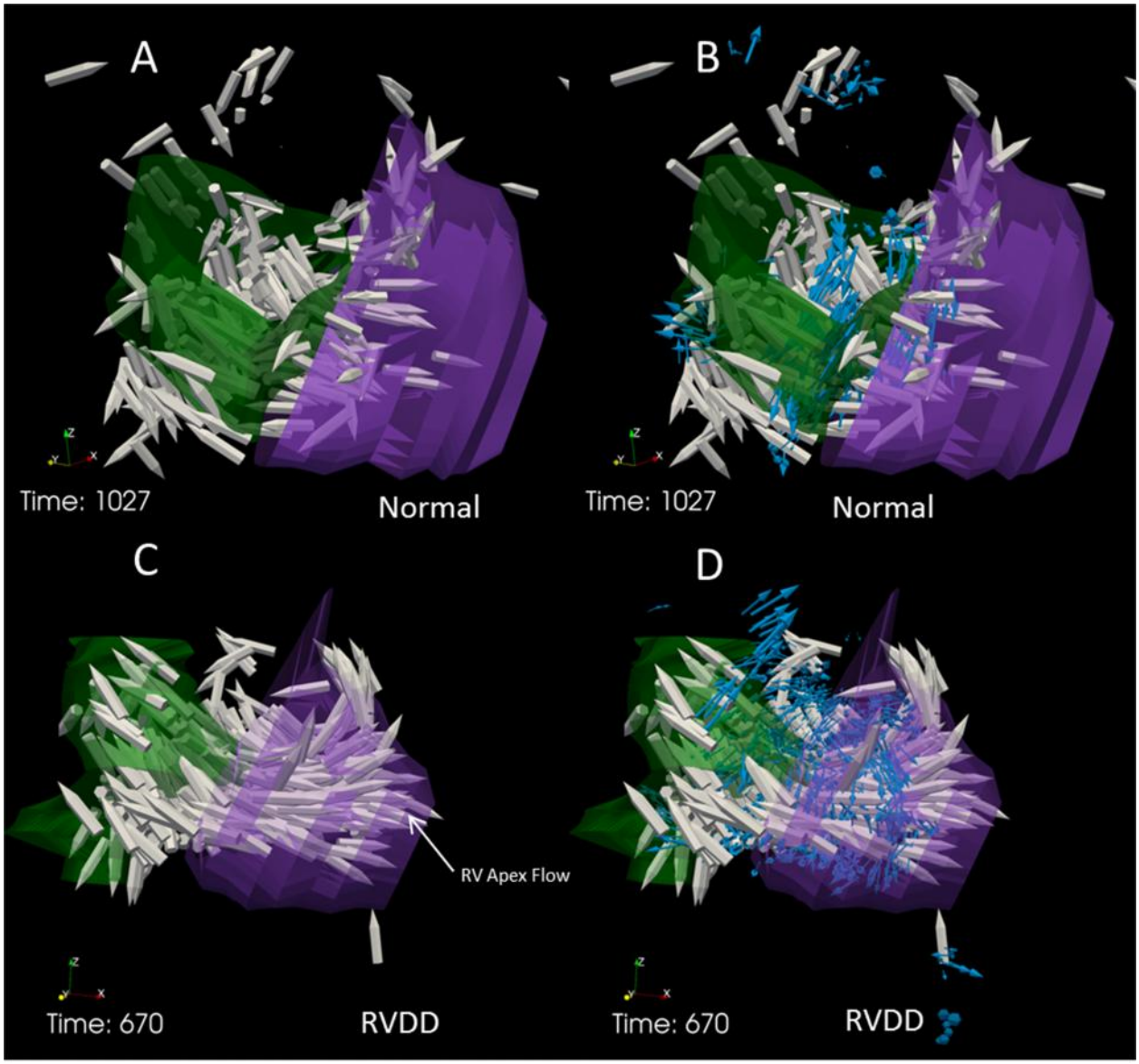

Figure 34. . Late diastolic flow visualization in the right heart for a normal and RVDD subject. Velocity vectors are shown in white, vorticity vectors are blue, and RV and RA endocardium segmentations are purple and green respectively.

6. Discussion

In this paper we detail a method for quantitatively examining early diastolic vorticity in the RA, RV and RH regions of the human heart. In order to arrive at a statistical analysis of the difference in spatially integrated vorticity between an RVDD population and controls, several intermediate steps are involved including data preprocessing and quality control, analysis of right heart cardiac event timing, development of a methodical workflow for defining the regions of interest, and assessing interobserver reliability.

4DMRI Data Characteristics

In-plane spatial resolution of 4DMRI resolution was found to range from 1.98-2.60 mm. while cine in-plane spatial resolution was 1.09 – 1.56 mm or roughly twice the linear resolution of 4DMRI images. The resolution of velocity images was adequate for visualization and analysis of large flow structures including fluid streams in the major arteries and veins (including the hepatic veins), helix structures in the RA, and fan-like inflows in the right ventricle. However, smaller and more subtle flow structures such as fluid wrapping around the TV leaflets potentially forming a true vortex ring were difficult to visualize given this spatial resolution. The higher spatial resolution of cine images allowed for more detailed locating of anatomical structures, however the temporal mismatch that occurs between velocity images and cine images can result in difficulties and inaccuracies in locating anatomical structures via cine images relative to velocity flow structures, particularly during periods of the cardiac structure in which the morphology of the right heart is varying quickly, such as the fast long-axis motion of the tricuspid annulus during early diastole. Temporal resolution was 50 ms for all 4DMRI images, while resolution ranged from 18-53 ms for cine images with a number of images per cardiac cycle of either 25 or 30. The 50 ms resolution of 4DMRI images does not allow for analysis of true peak early diastole or peak systole for all subjects due to the relatively short timespans of cardiac events. For example, from the MPA and

TV flowrate curves shown in Figure 20 it is seen that the entire systolic and early diastolic events last only roughly 300 ms, or only 6 times the length of the 4DMRI spatial resolution.

Nominal interval, a measure of heart rate during a given image acquisition within a 4DMRI/cine scan, was found to vary considerably within an individual cine image orientation (max variation = 38% of mean), and between average nominal interval for a cine orientation and associated 4DMRI data (max variation = 10.7%). This implies that temporal, and associated spatial, coregistration issues when working with both cine and 4DMRI data. In particular, variations in nominal interval within the various images for a given patient may partially explain the occasional instances of vectors seemingly passing through endocardium segmentations as seen in Figure 23.

Because 4DMRI and cine image acquisitions are prospectively and retrospectively gated respectively, 4DMRI MPA and TV flowrate curves were temporally integrated and compared for each subject to estimate the amount data truncation at the end of diastole. It was found that for all subjects, there was an average 5.0% diastolic flow volume through the TV compared to flow through MPA systolic flow. However, when broken into normal and RVDD groups, we found a 21.8% deficit in the normal group while the RVDD had an average of a 7.3% surplus. This may be explained by TV regurgitation which may be more prevalent in the RVDD group due to poor tricuspid valve performance originating from RH morphological changes coincident with cardiomyopathy. Regardless of the cause, the large average TV flow deficit in the normal group did not allow for quantitative analysis of late diastolic flow characteristics. Comparative visual/qualitative analysis was performed on an RVDD and normal subject who had clear late diastolic flowrate peaks in their respective TV flowrate curves.

Cardiac Event Timing

Due to the availability of reliable and automatic LV segmentation tools, time derivative of LV volume curves was found to be a practical method for estimating the timing of cardiac events in the normal left

heart including peak systole, and peak early and late diastole. Because reliable automatic segmentation of the left ventricle is not currently possible, a methodology was developed to estimate timing of cardiac events in the right heart which involved measuring flowrates through the TV and MPA. Due to limitations of spatial resolution, as well as significant heart rate variability within and between cine and 4DMRI image acquisitions, these methods were not found to be practical for assessing precise differences in cardiac event timing between the left and right heart for both RVDD and normal groups. It should be noted that both of these cardiac event timing methods require the assumption of no valvular regurgitation. In particular, translating LV volume to mitral valve and aortic flowrates becomes inaccurate in the presence of regurgitation.

RVDD subjects often present an additional challenge to estimating diastolic heart events due to a lack of distinct early and late diastolic peaks in the TV flowrate time series. However, by using the length of a pathologic subjects LV diastolic pause as a reference, and working backwards from peak RV late diastole, we were able to methodically assign a time for peak early diastole to patients without a clear early diastolic TV flowrate peak. The TV and MPA flowrate method was ultimately used to find peak early diastolic timing for all subjects.

Peak E-wave Vorticity

Interobserver variability of vorticity integration was assessed for a 23 subject subset of the cohort using two trained analysts. Because we theorized that thresholding the vorticity vectors prior to spatial integration would both focus the analysis on larger coherent flow structures in the right heart as well as reduce the dependency of the results on small differences in placement of the rectangular prismatic ROI, we calculated a concordance coefficient for several vorticity thresholds ranging from 0.005 to 0.01 s^{-1} (0.005 s^{-1} increments) and found that good agreement began with a threshold of roughly 0.04 s^{-1}, after which gains in agreement were minimal. To elucidate the dependency of interobserver reliability

on vorticity threshold, we examined images of early diastolic RH vorticity vectors for several threshold levels in a normal subject and observed that at a threshold of roughly 0.03-0.04 s^{-1} noise is reduced and flow structures gain visual coherence.

Spatially integrated early diastolic RH vorticity was compared between the RVDD and control groups using four methods of threshold and integrated vorticity scaling. Statistically significant differences were found for three of the methods, and the greatest significances generally occurred in the RA using thresholds ranging from 0.03 to 0.06 s^{-1} and both CI scaled integrated vorticity and CI scaled thresholds. No significant differences were found between the two groups when vorticity was not scaled. Less significant differences were found between the two groups when both the SS and TS scaling methods were used in conjunction. It is theorized that this "double" scaling only serves to convolute the results while a single scaling elucidates differences in vorticity between RVDD and controls by reducing the dependence of vorticity values on heart rate and heart volume. The highest significance, $p = 0.014$, occurred with a threshold of 0.04 s^{-1} and the SS scaling method. This result, together with the indication from the interobserver variability analysis, indicates that assessing peak spatially integrated vorticity using a threshold of 0.04 s^{-1} and scaling the results by CI may be the most promising vorticity metric for the study of RVDD pathology as well as the most promising RVDD metric for further investigation for clinical use.

Q-criterion and Lambda$_2$

Peak early diastolic Q-criterion and Lambda$_2$ was calculated within ParaView for each pixel within the identical rectangular prismatic RH and RV volumes used for vorticity analysis. T-tests between RVDD and normal groups were calculated for both straight volumes and volumes scaled by cine derived end diastolic volumes (RVEDV) and visualizations were developed for one RVDD and one normal subject. A significantly higher volume of Lambda$_2$ pixels occurred in the RH ROI in RVDD subjects versus normals.

However, there was not a comparable level of significance in either the RA or RV which may suggest that the manually placed plane separating the RA from the RV cuts through the region of $Lambda_2$ that is driving the statistical difference between RVDD and normal subjects which confounds the more spatially RA and RV analyses. When $lambda_2$ volume is scaled by RVEDV in an attempt to minimize the effect of RA and RV volume on the results, the statistical significance of the RH result is negated indicating that RVDD subjects in this cohort have larger RVEDV than normals. A two-tailed unequal variance t-test showed significantly higher RVEDV in RVDD subjects versus normals (Normal mean RVEDV = 138 ml, RVDD mean RVEDV = 182 ml, $p = 0.022$).

Visualizations of $lambda_2$ and Q-criterion in the right heart of both a normal and RVDD subject showed several interesting details of RH early diastolic flow as well as characteristics of the $lambda_2$ and Q-criterion analysis methods. In the normal, both methods indicated a clockwise helical flow in the RA and flow around the posterior TV leaflet, with the Q-criterion resulting in a smaller indicated vortex core within the helical flow. The criterion in the RVDD subject also indicated flow around the posterior leaflet, but rather than showing a helical vortex core in the RA, the RVDD appeared to have a broken or partial ring vortex core just downstream of the tricuspid valve in the region of the RV inflow. The addition of velocity vectors and streamlines to these visualizations confirmed these instantaneous flow structures indicated by the Q and $Lambda_2$ analysis. Although this RH $lambda_2$ and Q-criterion analysis was not shown to be a statistically significant indicator of RVDD in this cohort of subjects, it was shown to be an accurate and relatively easily implemented method for identification of 3D flow structures in the right heart using 4DMRI data despite limited spatial and temporal resolution.

Right Heart Flow Visualization

Flow visualizations were presented for an RVDD subject and a normal subject at peak systole, peak early diastole, and late diastole.

Three-dimensional systolic flow patterns showed similarities between the normal and RVDD subject including strong IVC and SVC flows meeting in the RA forming a right handed helix and encouraging IVC and SVC blood mixing, and a strong stream leaving the RV and entering the MPA via the RVOT. One difference was a clear hepatic flow meeting and wrapping clockwise around the main IVC flow just inferior to the RA.

At peak early diastole, IVC and SVC flow continues to enter the RA, but the hepatic flow seen in the normal subject is no longer visible. In both the normal RVDD subjects, a strong RV inflow is present, with the major difference being a clearly visible split of the RV inflow into a stream wrapping up towards the RVOT and pulmonary valve, and a separate smaller stream continuing towards the RV apex in the normal subject. This feature was not visible in the RVDD subject. It is hypothesized that the split may be due in part to the location of the papillary muscles in the normal subject and may also be due to more functional relaxation of the RV in the normal state. In both subjects, a ring of wall generated vorticity was observed at the TV annulus, with the RVDD ring intruding further along the RV long-axis. Again, this may be due to morphological changes coincident with advanced cardiomyopathy in the RVDD subject.

Late diastolic visualization showed the greatest disparity in 3D flow structures between the normal and RVDD subjects. IVC and SVC flow has mostly ceased in the normal subject, while in the RVDD subject significant retrograde flow is apparent in the both the IVC and SVC. It is hypothesized that this increase in retrograde flow in the RVDD subject compared to the normal is due to increased RH pressures coincident with the RVDD pathology. The late diastolic RV inflow is significantly stronger in the RVDD subject than the normal subject due to the late diastolic atrial contractile RV filling predominance over early diastolic RV relaxation filling which is not present in the normal subject. In the RVDD subject, the RV inflow stream now begins to split into an RVOT stream and a stream continuing towards the RV apex as was seen in the normal subject during early diastole.

Acknowledgements

This research has been funded by Siemens AG and the Butcher Foundation. The work was done in collaboration with the research groups of Dr. Brett Fenster of National Jewish Health and the University of Colorado School of Medicine and Dr. Joyce Schroeder, of the University of Colorado Denver School of Medicine. Jean Hertzberg, PhD is the advisor for this project.

References

Barker, Alex J., Craig Lanning, and Robin Shandas. 2009. “Quantification of Hemodynamic Wall Shear Stress in Patients with Bicuspid Aortic Valve Using Phase-Contrast MRI.” *Annals of Biomedical Engineering* 38 (3): 788–800. doi:10.1007/s10439-009-9854-3.

Bieging, Erik T., Alex Frydrychowicz, Andrew Wentland, Benjamin R. Landgraf, Kevin M. Johnson, Oliver Wieben, and Christopher J. François. 2011. “In Vivo Three-Dimensional MR Wall Shear Stress Estimation in Ascending Aortic Dilatation.” *Journal of Magnetic Resonance Imaging* 33 (3): 589–97. doi:10.1002/jmri.22485.

Bock, J., BW Kreher, J. Hennig, and M. Markl. 2007. “Optimized Pre-Processing of Time-Resolved 2D and 3D Phase Contrast MRI Data.” In *Proceedings of the 15th Annual Meeting of ISMRM, Berlin, Germany*, 3138.

Bogren, Hugo G., and Michael H. Buonocore. 2010. “Helical-Shaped Streamlines Do Not Represent Helical Flow.” *Radiology* 257 (3): 895–96. doi:10.1148/radiol.101298.

Bolger, Ann F, Einar Heiberg, Matts Karlsson, Lars Wigström, Jan Engvall, Andreas Sigfridsson, Tino Ebbers, John-Peder Escobar Kvitting, Carl Johan Carlhäll, and Bengt Wranne. 2007. “Transit of Blood Flow through the Human Left Ventricle Mapped by Cardiovascular Magnetic Resonance.” *Journal of Cardiovascular Magnetic Resonance: Official Journal of the Society for Cardiovascular Magnetic Resonance* 9 (5): 741–47. doi:10.1080/10976640701544530.

Bollache, Emilie, Alban Redheuil, Stéphanie Clément-Guinaudeau, Carine Defrance, Ludivine Perdrix, Magalie Ladouceur, Muriel Lefort, Alain De Cesare, Alain Herment, and Benoît Diebold. 2010. “Automated Left Ventricular Diastolic Function Evaluation from Phase-Contrast Cardiovascular Magnetic Resonance and Comparison with Doppler Echocardiography.” *J Cardiovasc Magn Reson* 12: 63.

Chatterjee, Kanu, and Barry Massie. 2007. “Systolic and Diastolic Heart Failure: Differences and Similarities.” *Journal of Cardiac Failure* 13 (7): 569–76. doi:10.1016/j.cardfail.2007.04.006.

ElBaz, Mohammed S., Emmeline Calkoen, Jos J. Westenberg, Boudewijn PF Lelieveldt, Arno Roest, and Rob J. van der Geest. 2014. “Three Dimensional Right Ventricular Diastolic Vortex Rings: Characterization and Comparison with Left Ventricular Diastolic Vortex Rings from 4D Flow MRI.” *Journal of Cardiovascular Magnetic Resonance* 16 (Suppl 1): P42. doi:10.1186/1532-429X-16-S1-P42.

Eriksson, J., C.J. Carlhall, P. Dyverfeldt, J. Engvall, A.F. Bolger, and T. Ebbers. 2010. “Semi-Automatic Quantification of 4D Left Ventricular Blood Flow.” *Journal of Cardiovascular Electrophysiology*, J. Cardiovasc. Electrophysiol. (USA), 12 (6-9): 10 pp.

Fenster, B.E., James Browning, Joyce D. Schroeder, Michal Schafer, Chris A. Podgorski, Jamie Smyser, Lori J. Silveira, J. Kern Buckner, and Jean R. Hertzberg. 2015. “Vorticity Is a Marker of Right Ventricular Diastolic Dysfunction.” *American Journal of Physiology - Heart and Circulatory Physiology* 309 (6): H1087–93. doi:10.1152/ajpheart.00278.2015.

Fenster, Brett. 2011Personal Interview.

Francois, C. J., S. Srinivasan, M. L. Schiebler, S. B. Reeder, E. Niespodzany, B. R. Landgraf, O. Wieben, and A. Frydrychowicz. 2012. “4D Cardiovascular Magnetic Resonance Velocity Mapping of Alterations of Right Heart Flow Patterns and Main Pulmonary Artery Hemodynamics in Tetralogy of Fallot.” *Journal of Cardiovascular Magnetic Resonance* 14 (1): 16.

Fredriksson, Alexandru G., Jakub Zajac, Jonatan Eriksson, Petter Dyverfeldt, Ann F. Bolger, Tino Ebbers, and Carl-Johan Carlhäll. 2011. “4-D Blood Flow in the Human Right Ventricle.” *American Journal of Physiology - Heart and Circulatory Physiology* 301 (6): H2344–50. doi:10.1152/ajpheart.00622.2011.

Geiger, J., M. Markl, B. Jung, J. Grohmann, B. Stiller, M. Langer, and R. Arnold. 2011. “4D-MR Flow Analysis in Patients after Repair for Tetralogy of Fallot.” *European Radiology* 21 (8): 1651–57. doi:10.1007/s00330-011-2108-4.

Haddad, François, Ramona Doyle, Daniel J. Murphy, and Sharon A. Hunt. 2008. “Right Ventricular Function in Cardiovascular Disease, Part II Pathophysiology, Clinical Importance, and Management of Right Ventricular Failure.” *Circulation* 117 (13): 1717–31. doi:10.1161/CIRCULATIONAHA.107.653584.

Heiberg, E., L. Wigstrom, M. Carlsson, A.F. Bolger, and M. Karlsson. 2005. “Time Resolved Three-Dimensional Automated Segmentation of the Left Ventricle.” In *Computers in Cardiology, 2005*, 599–602. doi:10.1109/CIC.2005.1588172.

Henderson, Amy. 2004. *The ParaView Guide: A Parallel Visualization Application*. Clifton Park, NY: Kitware.

Heron, M., D.L. Hoyert, S.L. Murphy, J. Xu, K.D. Kochanek, and B. Tejada-Vera. 2015. “National Vital Statistics Reports.” *National Vital Statistics Reports* 64 (10).

Hope, Michael D, Thomas A Hope, Alison K Meadows, Karen G Ordovas, Thomas H Urbania, Marcus T Alley, and Charles B Higgins. 2010. “Bicuspid Aortic Valve: Four-Dimensional MR Evaluation of Ascending Aortic Systolic Flow Patterns.” *Radiology* 255 (1): 53–61. doi:10.1148/radiol.09091437.

Hope, Michael D., Alison K. Meadows, Thomas A. Hope, Karen G. Ordovas, Gautham P. Reddy, Marcus T. Alley, and Charles B. Higgins. 2008. “Evaluation of Bicuspid Aortic Valve and Aortic Coarctation With 4D Flow Magnetic Resonance Imaging.” *Circulation* 117 (21): 2818–19. doi:10.1161/CIRCULATIONAHA.107.760124.

Jeong, Jinhee, and Fazle Hussain. 1995. “On the Identification of a Vortex.” *Journal of Fluid Mechanics* 285: 69–94.

Jiang, Ming, Raghu Machiraju, and David Thompson. 2005. “Detection and Visualization of Vortices.” In *The Visualization Handbook*, 295–309. Academic Press.

Kilner, P J, G Z Yang, A J Wilkes, R H Mohiaddin, D N Firmin, and M H Yacoub. 2000. “Asymmetric Redirection of Flow through the Heart.” *Nature* 404 (6779): 759–61. doi:10.1038/35008075.

Maceira, Alicia M, Sanjay K Prasad, Mohammed Khan, and Dudley J Pennell. 2006. “Reference Right Ventricular Systolic and Diastolic Function Normalized to Age, Gender and Body Surface Area from Steady-State Free Precession Cardiovascular Magnetic Resonance.” *European Heart Journal* 27 (23): 2879–88. doi:10.1093/eurheartj/ehl336.

Markl, Michael. 2005. “Velocity Encoding and Flow Imaging.” *University Hospital Frieberg*.

Markl, Michael, Frandics P. Chan, Marcus T. Alley, Kris L. Wedding, Mary T. Draney, Chris J. Elkins, David W. Parker, et al. 2003. “Time-Resolved Three-Dimensional Phase-Contrast MRI.” *Journal of Magnetic Resonance Imaging: JMRI* 17 (4): 499–506. doi:10.1002/jmri.10272.

Markl, Michael, Julia Geiger, Philip J. Kilner, Daniela Föll, Brigitte Stiller, Friedhelm Beyersdorf, Raoul Arnold, and Alex Frydrychowicz. 2011. “Time-Resolved Three-Dimensional Magnetic Resonance Velocity Mapping of Cardiovascular Flow Paths in Volunteers and Patients with Fontan Circulation.” *European Journal of Cardio-Thoracic Surgery* 39 (2): 206–12. doi:10.1016/j.ejcts.2010.05.026.

Markl, Michael, Philip Kilner, and Tino Ebbers. 2011. “Comprehensive 4D Velocity Mapping of the Heart and Great Vessels by Cardiovascular Magnetic Resonance.” *Journal of Cardiovascular Magnetic Resonance* 13 (1): 7. doi:10.1186/1532-429X-13-7.

McLaughlin, Vallerie V., Stephen L. Archer, David B. Badesch, Robyn J. Barst, Harrison W. Farber, Jonathan R. Lindner, Michael A. Mathier, et al. 2009. “ACCF/AHA 2009 Expert Consensus Document on Pulmonary HypertensionA Report of the American College of Cardiology Foundation Task Force on Expert Consensus Documents and the American Heart Association

Developed in Collaboration With the American College of Chest Physicians; American Thoracic Society, Inc.; and the Pulmonary Hypertension Association." *Journal of the American College of Cardiology* 53 (17): 1573–1619. doi:10.1016/j.jacc.2009.01.004.

McRobbie, Donald W., Elizabeth A. Moore, Martin J. Graves, and Martin R. Prince. 2006. *MRI from Picture to Proton*. Second edition. Cambridge University Press. http://dx.doi.org/10.1017/CBO9780511545405.

Moran, P R. 1982. "A Flow Velocity Zeugmatographic Interlace for NMR Imaging in Humans." *Magnetic Resonance Imaging* 1 (4): 197–203.

Pal, Prasanta, Ziheng Zhang, Ben A Lin, Donald Dione, Albert J Sinusas, and Smita Sampath. 2012. "Flow Vortex Quantification in the Left Atrium." *Journal of Cardiovascular Magnetic Resonance* 14 (Suppl 1): W23. doi:10.1186/1532-429X-14-S1-W23.

Petitjean, Caroline, and Jean-Nicolas Dacher. 2011. "A Review of Segmentation Methods in Short Axis Cardiac MR Images." *Medical Image Analysis* 15 (2): 169–84. doi:10.1016/j.media.2010.12.004.

Rodriguez Munoz, D., M. Markl, J. L. Moya Mur, A. Barker, C. Fernandez-Golfin, P. Lancellotti, and J. L. Zamorano Gomez. 2013. "Intracardiac Flow Visualization: Current Status and Future Directions." *European Heart Journal - Cardiovascular Imaging* 14 (11): 1029–38. doi:10.1093/ehjci/jet086.

Roldán-Alzate, A., H. B. Kellihan, D. W. Consigny, E. J. Niespodzany, C. J. François, O. Wieben, N. C. Chesler, and A. Frydrychowicz. 2011. "4D MR Velocity Mapping Using PC VIPR to Investigate the Hemodynamics of Acute Pulmonary Hypertension in a Dog Model." In *Proc. Intl. Soc. Mag. Reson. Med.*, 19:1326. http://www.google.com/url?sa=t&rct=j&q=&esrc=s&source=web&cd=1&ved=0CGIQFjAA&url=http%3A%2F%2Fsubmissions.miracd.com%2Fismrm2011%2Fproceedings%2Ffiles%2F1326.pdf&ei=umghUK7vD8jY2gWK3oHACQ&usg=AFQjCNFuA0zOtWiS1MTXOZxuQDhi_vFfuQ&sig2=FL8tZ4o3iS85btw1nSxVcg.

Rudski, Lawrence G, Wyman W Lai, Jonathan Afilalo, Lanqi Hua, Mark D Handschumacher, Krishnaswamy Chandrasekaran, Scott D Solomon, Eric K Louie, and Nelson B Schiller. 2010. "Guidelines for the Echocardiographic Assessment of the Right Heart in Adults: A Report from the American Society of Echocardiography Endorsed by the European Association of Echocardiography, a Registered Branch of the European Society of Cardiology, and the Canadian Society of Echocardiography." *Journal of the American Society of Echocardiography: Official Publication of the American Society of Echocardiography* 23 (7): 685–713; quiz 786–88. doi:10.1016/j.echo.2010.05.010.

"RV Segmentation Challenge in Cardiac MRI — Litislab." 2012. http://www.litislab.eu/rvsc/workshop/rv-segmentation-challenge-in-cardiac-mri.

Schwarz, Ernst R, and Raja Dashti. 2010. "The Clinical Quandary of Left and Right Ventricular Diastolic Dysfunction and Diastolic Heart Failure." *Cardiovascular Journal of Africa* 21 (4): 212–20. doi:10.5830/CVJA-2010-018.

Toger, Johannes, Mikael Kanski, Marcus Carlsson, Sandor J Kovacs, Gustaf Soderlind, Hakan Arheden, and Einar Heiberg. 2012. "Diastolic Vortex Ring Formation in the Human Left Ventricle: Quantitative Analysis Using Lagrangian Coherent Structures and 4D Cardiovascular Magnetic Resonance Velocity Mapping." *Journal of Cardiovascular Magnetic Resonance* 14 (Suppl 1): W30. doi:10.1186/1532-429X-14-S1-W30.

"Types of Heart Failure." 2014. Accessed April 13. http://www.heart.org/HEARTORG/Conditions/HeartFailure/AboutHeartFailure/Types-of-Heart-Failure_UCM_306323_Article.jsp.

Voelkel, Norbert F., Robert A. Quaife, Leslie A. Leinwand, Robyn J. Barst, Michael D. McGoon, Daniel R. Meldrum, Jocelyn Dupuis, et al. 2006. "Right Ventricular Function and Failure Report of a National Heart, Lung, and Blood Institute Working Group on Cellular and Molecular Mechanisms

of Right Heart Failure." *Circulation* 114 (17): 1883–91. doi:10.1161/CIRCULATIONAHA.106.632208.

Walker, Peter G, Gregory B Cranney, Markus B Scheidegger, Gena Waseleski, Gerald M Pohost, and Ajit P Yoganathan. 1993. "Semiautomated Method for Noise Reduction and Background Phase Error Correction in MR Phase Velocity Data." *Journal of Magnetic Resonance Imaging* 3 (3): 521–30. doi:10.1002/jmri.1880030315.

Yu, C. M., J. E. Sanderson, Skiva Chan, Leata Yeung, Y. T. Hung, and K. S. Woo. 1996. "Right Ventricular Diastolic Dysfunction in Heart Failure." *Circulation* 93 (8): 1509–14. doi:10.1161/01.CIR.93.8.1509.

Zuluaga, Maria A., M. Jorge Cardoso, Marc Modat, and Sébastien Ourselin. 2013. "Multi-Atlas Propagation Whole Heart Segmentation from MRI and CTA Using a Local Normalised Correlation Coefficient Criterion." In *Proceedings of the 7th International Conference on Functional Imaging and Modeling of the Heart*, 174–81. FIMH'13. Berlin, Heidelberg: Springer-Verlag. doi:10.1007/978-3-642-38899-6_21.

Appendix A Lambda$_2$ ParaView/Python script

Filter: Merge Blocks

Filter: Gradient of Unstructured Data Set (Scalar Array: velocity. Also checkbox compute Q-criterion if desired)

Filter: Programmable Filter, then in script field:

```
import numpy
grads = inputs[0].PointData['Gradients']
size_grads = shape(grads)
second_eig = numpy.zeros((size_grads[0],1))
for x in range(0, size_grads[0]):
 tensor = numpy.matrix.transpose(grads[x,:,:])
 symm_mat = 0.5*(tensor+numpy.matrix.transpose(tensor))
 anti_mat = 0.5*(tensor-numpy.matrix.transpose(tensor))
 s_square = numpy.dot(symm_mat,symm_mat)
 a_square = numpy.dot(anti_mat,anti_mat)
 lambda2_mat = s_square+a_square
 eigs = numpy.linalg.eigvals(lambda2_mat)
 eigs_sort = numpy.sort(eigs)
 second_eig[x] = eigs_sort.item(1)
output.PointData.append(second_eig[:], "Lambda2")
```